ABSTRACT

Title of Document: ADHESION STRENGTH MEASUREMENT OF MULTILAYER STRUCTURES WITH VERTICAL CRACK BY FOUR POINT BENDING TEST

Stephen Junho Kang
Master of Science
2014

Directed By: Professor Bongtae Han
Department of Mechanical Engineering

Current microelectronic packages consist of multilayer systems. Adhesion strength is one of the most important factors to the reliability of these systems. Previous studies have used four point bending tests as a method for characterizing the energy release rate to obtain the adhesion strength of bilayer systems. An extension of this work is proposed in this study, where a four point bending test of multilayer structures with a vertical crack is used to measure the adhesion strength, assisted by the presence of a predefined area. The predefined area allows for a weak adhesion horizontal accurate pre-crack which permits crack propagation under loading as well as reducing scatter within the values of critical loads. A numerical analysis is conducted to compute the energy release rate from the critical loads using the concept of the J-integral. Two sets of multilayer specimens were fabricated and tested in the study: one for investigating crack front behavior relative to the compliance change in the load-displacement profile by using transparent substrates, and the other using the previous set as a guideline for testing metal substrates under certain environmental

conditions. Experimental results along with visual evidence support the consistent behavior between crack front behavior and compliance change. This correlation can be used as a baseline for testing other electronic packages for interfacial failure.

ADHESION STRENGTH MEASUREMENT OF MULTILAYER STRUCTURES WITH VERTICAL CRACK BY FOUR POINT BENDING TEST

By

Stephen Junho Kang

Thesis submitted to the Faculty of the Graduate School of the
University of Maryland, College Park, in partial fulfillment
of the requirements for the degree of
Master of Science
2014

Advisory Committee:
Professor Bongtae Han, Chair
Professor Patrick McCluskey
Research Professor Yunho Hwang

ACKNOWLEDGEMENTS

I wanted to first and foremost give my utmost gratitude to my advisor, Dr. Bongtae Han. Dr. Bongtae Han, your mentoring, leadership, and fatherly care was truly significant in finalizing my research work. Through the years of face to face conversations about research and personal guidance, I will never forget those words which will help me strive for greater success. I would like to thank you again for taking me under your wing as well as your great patience and consideration which helped me build who I am today.

In addition, I would like to thank Dr. Patrick McCluskey and Dr. Yunho Hwang for serving on my thesis committee.

With regards to my research development and peer guidance, I would like to give my huge gratitude to my lab partner, Kenny Mahan. You are truly one helpful, patient, and excellent friend and peer that I had beside me in the lab. Thank you for your guidance and assistance with my research including sample preparation, modeling, background education, and thesis preparation. As for my lab group members, I would like to thank you all for your advice and presence especially to Michelle Kim, Dae-Suk Kim, Yong Sun, David Rosen, Sean Wei, Bulong Wu, Brian Kwong, Dr. Hyunseok Oh, and Bongmin Song. I shall not forget our friendships and times we have spent together in the lab. In addition, I would like to thank Aroom for his big

help in the machine shop which allowed me to progress in my research in terms of sample preparation.

Thank you to my hard working and supportive parents, my little brother, and my beloved grandmother. You all have been very supportive, patient, and persevering through the times I have been in graduate school. I will continue to learn and feed off your love to become stronger and overcome the obstacles that I may face.

Finally, friends and Voices As One Youth Church Choir, I want to thank you all for being there for me with inspiration, love, and joy which helped me go through with this research. Thank you everyone for making this possible.

TABLE OF CONTENTS

LIST OF TABLES

LIST OF FIGURES

CHAPTER 1: BACKGROUND AND MOTIVATION

1.1 *Reliability of microelectronics packaging*

Microelectronics is common throughout everywhere in this ever changing evolving world integrated with technology. In these typical microelectronic packages, interfaces and multilayers are ubiquitous in which play a pivotal role in terms of functionality for interconnects and packaging structures. However, as these packages are utilized everyday under a variety of surroundings such as harsh environments, reliability issues arise such as delamination and fracture. New materials and processes develop since functionality of devices continue to increase which makes reliability control more challenging and eye catching to research. Evaluating interfacial delamination becomes one of the major concerns in terms of performance and reliability which demands prediction of interface reliability with cost and time effective testing. In addition, having a fundamental understanding of interface adhesion can deliver direction for developing new materials and processes to improve interface reliability.

Microelectronic packages are establishments of electrical interconnections and housing for integrated circuits made up of organic and inorganic materials [1]. Such examples of interfaces in today' semiconductor packages include epoxy molding compounds, silicon chips, dielectric materials, solder resist, underfill/die attach, and print circuit boards. These materials with varying mechanical properties such as moduli and coefficients of thermal expansion (CTEs) help induce failure mechanisms in such microelectronic packages that lead to interfacial delamination and fracture. There are numerous interfaces in electronic packages in which each are a potential

reliability concern. Certain factors of interfacial delamination caused by harsh environments are to be discussed in which stresses affect the adhesive bond interface in packages.

1.2 *Factors of interfacial delamination in microelectronic packages*

1.2.1 Coefficient of Thermal Expansion (CTE) mismatch

One of the major factors for interfacial delamination in microelectronic packages is the mismatch between the different material properties such as the coefficient of thermal expansion (CTE). Such material like a plastic bonded to a material with a large difference in CTE such as a metal, very high or very low temperatures may induce stress and strain conditions at the interface which leads to fracture or separation of the bond [2]. With the temperature falling well below room temperature, a plastic bonded to a metal would shrink more than its counterpart which loosens the bond. In addition, high temperature may enhance migration of a chemical in the plastic to the bonded interface which reduces bond strength. For typical encapsulated devices, a polymer generally transfers stresses from a low-expansion silicon chip to a high-expansion printed circuit board.

1.2.2 Hygroscopic swelling

Along with the CTE mismatch in a bonded microelectronic package, hygroscopic swelling is another failure phenomenon which induces premature interfacial delamination. In a typical microelectronic package, once moisture is absorbed, hygroscopic stresses ascend when polymeric materials swells upon absorbing moisture whereas the non-polymeric materials such as the lead frame, die

paddle and silicon die do not experience any swelling. Hygroscopic swelling of a typical polymeric material such as an EMC, epoxy molding compound, acts as a mechanism which affects the warpage direction of a package by introducing moisture induced expansion to the EMC [3]. This phenomenon leads to hygroscopic mismatch stresses and strains in the package. In like comparison with the CTE mismatch, the hygroscopic stress increases as the swelling coefficient of a polymeric material increases which then decreases the adhesion strength between two materials leading to unwanted interfacial delamination.

1.2.3 Vapor pressure

In relation to hygroscopic swelling, water vapor pressure behaves as an external loading at interfaces when delamination occurs. When an electronic package undergoes preconditioning, polymeric materials in the package absorb moisture from the surroundings, which condenses into micro pores in these materials. With these micro pores, interfacial adhesion strength is degraded, specifically, at a high temperature level [3]. Condensed moisture is vaporized when the temperature rises during reflow, generating high internal vapor pressure inside of the package. This internal vapor pressure induces rapid growth of voids and defects along the interfaces which results in delamination. The package will then bulge with the help of vaporizing moisture which immediately exerts a pressure that acts as a traction loading at the delaminated interface. In addition to thermal expansion, vapor pressure induced expansion affects Young's modulus of plastic materials by a few orders at reflow temperature in which introduces additional mismatch [4]. As another note, vapor pressure saturates more rapidly than moisture which suggests that vapor

pressure can be uniformly distributed in polymeric material regardless of moisture saturation.

1.2.4 Moisture degradation

In addition to hygroscopic swelling and vapor pressure, delamination failures induced by moisture degradation also creates great concern for common microelectronic packaging such as flip chip interconnects. Moisture absorption in adhesive joints causes degradation of the adhesion strength and interfacial fracture toughness. Studies have shown that moisture can affect the interface physically by being present as well as changing the mechanical properties of the adhesive and substrate due to moisture uptake [5]. An adhesive structure affected by moisture absorption and diffusion over time and temperature can respond differently to the presence of an externally applied load. The effect of moisture absorption onto the interface can also be viewed upon the rate at which moisture is diffused and the rate at which adhesion strength is degraded.

1.2.5 Contaminated surface/surface roughness

Contaminated surfaces and surface roughness can factor in as one of the physical effects of materials that can lead to interfacial delamination. As an example, traces of contaminants such as oil on metals onto polymeric materials can cause low and variable adhesion. Silicone contamination has been a recurring reliability issue that reduces adhesion strength of organic adhesives used in the assembly and packaging of microelectronics devices [6]. These silicones have excellent chemical resistance and also prevent the direct contact between the adhesive and the adherend.

In addition, surface roughness comes into play in which adhesion also depends on how roughly treated is the surface of a substrate bonded to a polymeric material. For example, a study has shown that the higher adhesion constancy of a roughened copper substrate during temperature/humidity exposure may be caused by the physical inter-lock bonding [7]. A combination of surface roughening and chemical treatment can maintain and induce better adhesion strength between two materials.

1.3 *Terminology and mechanisms of adhesion*

One of the classic failure mechanisms that occur in plastically encapsulated microelectronics from adhesion is delamination. If one material such as a coating is applied to another material used as a substrate, adhesion is created. However, when the coating separates from its substrate, this is called delamination or decohesion. Once delamination occurs, one can measure the nature of delamination which is the adhesion strength [8]. Adhesion strength is a bimaterial property that indicates the bimaterial layer's resistance to delamination. The adhesion strength or bond strength is a significant factor in microelectronic and photonic packaging in which measurement is particularly challenging in which miniaturized bonds are utilized. The adhesion strength within an electronic package has its purpose to solely tolerate thermo-mechanical and mechanical stresses during manufacturing and service use. By quantifying adhesion strength in a reproducible and effective manner, this can help evaluate and investigate failure occurrences in a microelectronic package. However there are factors that instigate these challenges and influence test selection which include: type of interface such as thin film, multilayer stacks, and other configurations, amount of mixed-mode loading in applications, modulus ratio and

thickness ratio, rigidity, flexibility, and strength of materials used. Depending on these factors and specimen configuration that influence test selections, one test can prove to help quantify the adhesion strength. The main focus of this thesis is to address and help quantify adhesion strength by defining a test method along with understanding the basic fundamentals of delamination.

1.4 *Quantifying adhesion strength*

1.4.1 Stress intensity factor

One of the main focuses in this paper is how a structure behaves when a crack is existent along with the question of what happens at the tip of a crack. The answer lies on the singular stress concept in which deals with what is happening at the crack front/tip. At a crack tip, there is a stress concentration that is introduced in which takes the form of a square root singularity around crack tips. The forms of the singular field are universal to cracked bodies, regardless of shape and crack as shown below in Figure 1:

$$\sigma_{ij} = \frac{K}{\sqrt{2\pi r}} f_{ij}(\theta) \tag{1.4.1}$$

$$K = \sigma\sqrt{\pi a} \tag{1.4.2}$$

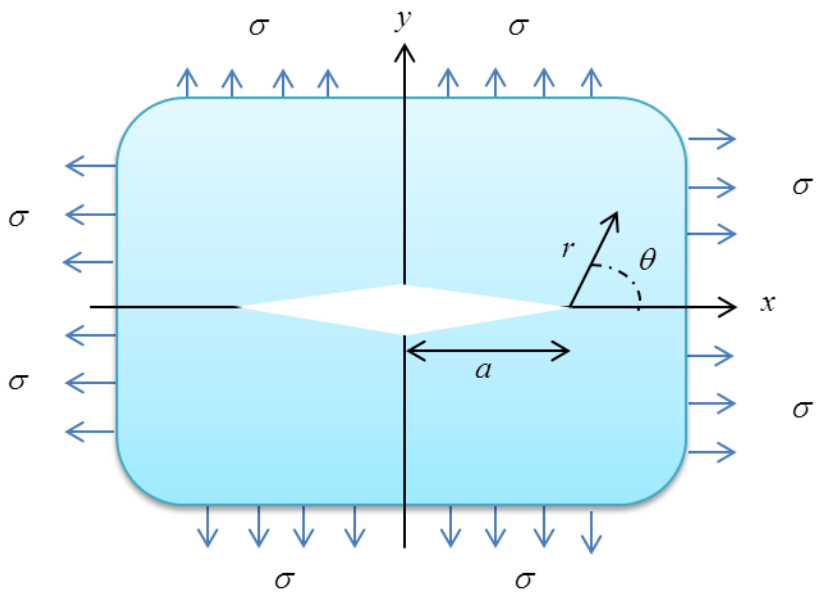

Figure 1.Through-thickness crack in an infinite plate loaded in biaxial tension

where the factor, *K*, called the stress intensity factor in the units of $MPa-\sqrt{m}$, completely describes the crack-tip conditions in a linear elastic material with other parameters such as the stress component, σ_{ij}, the radial coordinate measured from crack tip, *r*, the angular coordinate about the crack tip, θ, geometric factor that depends on load, $f_{ij}(\theta)$, and the crack length , *a* [9]. In other words, *K* gives out a description of how strong the stress field is near the crack tip. The reciprocal square root reliance of the stress components of r defines the singular behavior of the crack tip. The stability of the crack is expressed in terms of *K* in which follows a criteria below [10]:

$$\begin{aligned} K_I &< K_{I_C} \\ K_I &= K_{I_C} \\ K_I &> K_{I_C} \end{aligned} \tag{1.4.3}$$

where K_{IC}, the critical fracture toughness, is the determining factor whether a crack is arrested or cause catastrophic failure [11]. In respective to each criteria above: the first will have the crack stabilized if $K_I < K_{IC}$, the second will have marginal stability as $K_I = K_{IC}$, and finally the last case will produce unstable crack propagation where $K_I > K_{IC}$. [10] From the criteria of different K conditions, the crack propagates that starts with a displacement near the crack tip that varies with $\sqrt{r}$ with the addition of the stress varying with $1/\sqrt{r}$ which formulates singular field shown previously in Eqn.(1.4.1).

The behavior of the stress field near the crack tip will act differently and form different types of fracture depending on certain loading conditions shown below in Figure 2:

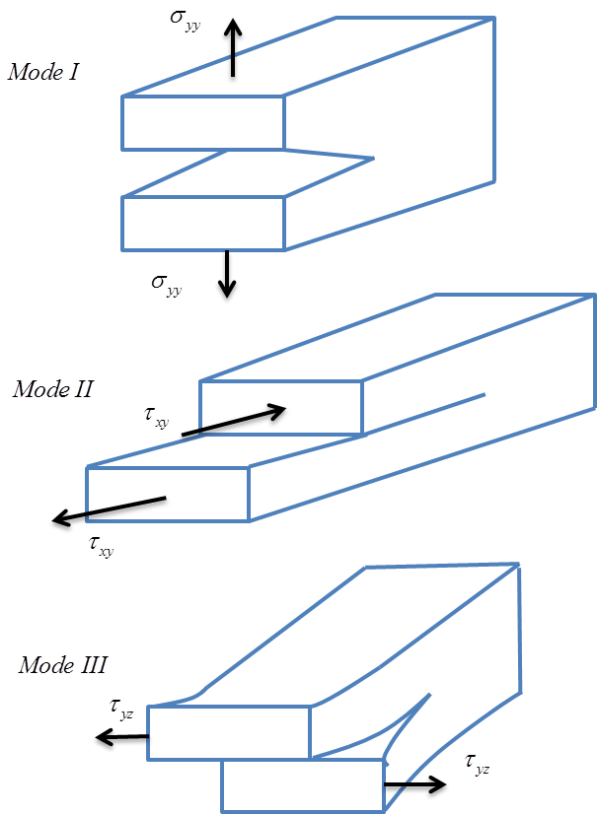

Figure 2.Three basic modes of loading of crack propagation: Mode I (tensile mode or opening), Mode II (in-plane shear or sliding mode), and Mode III (out-of-plane shear or tearing mode)

These three modes of crack propagation have their own specific stress intensity factors K_I, K_{II}, K_{III} correspondingly in which the subscripts are given to denote the mode [9]. Stress fields ahead of the crack tip of each mode in a linear elastic isotropic material are depicted below which corresponds to Eqn.(1.4.4) :

$$\lim_{r\to 0}\sigma_{ij}^{(I)} = \frac{K_I}{\sqrt{2\pi r}} f_{ij}^{(I)}(\theta)$$
$$\lim_{r\to 0}\sigma_{ij}^{(II)} = \frac{K_{II}}{\sqrt{2\pi r}} f_{ij}^{(II)}(\theta) \qquad (1.4.4)$$
$$\lim_{r\to 0}\sigma_{ij}^{(III)} = \frac{K_{III}}{\sqrt{2\pi r}} f_{ij}^{(III)}(\theta)$$

However when a combination of loading conditions are applied, this is known as Mixed-Mode fracture. The stress intensity factor describes the magnitude of the crack tip singularity in which stresses near the crack tip increase in proportion to the stress intensity factor, *K*. [12]As stress fields are concerned, there is another parameter in which relates itself with the stress intensity factor by quantifying the overall net change in potential energy that supplements an increment of crack extension known as the energy release rate.

1.4.2 Energy release rate

The energy release rate [12] explains the energy dissipation in which a solid is fractured which enough energy is sufficient in order to propagate a crack since new surface area is created by this:

$$G = -\frac{d\Pi}{dA} = -\frac{1}{w}\frac{dU}{da} \tag{1.4.5}$$

$$\Pi = U - W \tag{1.4.6}$$

G, the energy release rate, proposed by Irwin and extended from Griffith, is defined as the driving force present within the solid caused by accumulated elastic energy for propagating an existing crack shown in Eqn.(1.4.5). The potential energy of an elastic body, Π, is defined as the difference between the strain energy stored in the body, *U*, and the work done by external forces, *W*, as shown in Eqn.(1.4.6). The Griffith criterion from this energy release rate form can be portrayed in terms of crack length and constant stress of an infinitely wide plate with a through-thickness crack [12]. The energy release rate in this case can be expressed as:

$$-\frac{d\Pi}{dA}=\frac{\pi\sigma^2 a}{E} \tag{1.4.7}$$

Both the Irwin and Griffith criterion display respective representations of the energy release rate in which relates to one another under similar configurations. Thus, the energy release rate can be viewed in two tests: load controlled and displacement controlled.

1.4.3 Displacement control vs. load control testing

If one considers a cracked plate at a fixed load, shown in Figure 3, this is considered as a load controlled test.

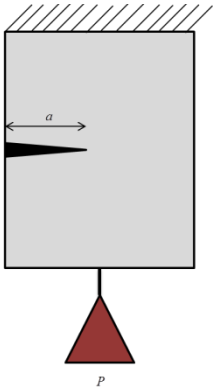

Figure 3.Cracked plate at fixed load

In order to fully understand this basic type of configuration, the work done by external forces in which this case:

$$W=P\Delta \tag{1.4.8}$$

with

$$U=\int_0^{\Delta} Pd\Delta=\frac{P\Delta}{2} \tag{1.4.9}$$

in which the potential energy stored in the body, Π, is equal to $-U$. The energy release rate or fracture energy is therefore provided by:

$$G = \frac{1}{B}\left(\frac{dU}{da}\right)_P = \frac{P}{2B}\left(\frac{d\Delta}{da}\right)_P \tag{1.4.10}$$

Graphically, as shown in Figure 4, in load control, the crack extension of *da* results in a net increase in strain energy due to external load *P*. [12]

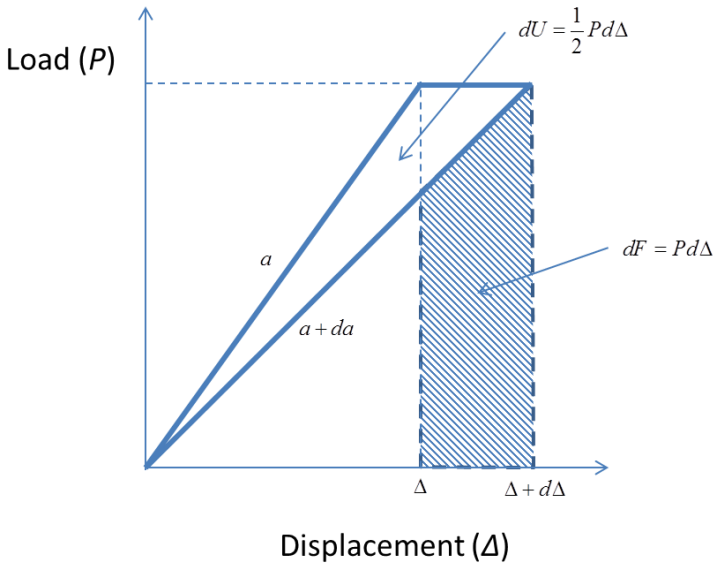

Figure 4.Graphical representation of load controlled test

However when the cracked plate is at a fixed displacement shown below in Figure 5, this is considered as a displacement controlled test.

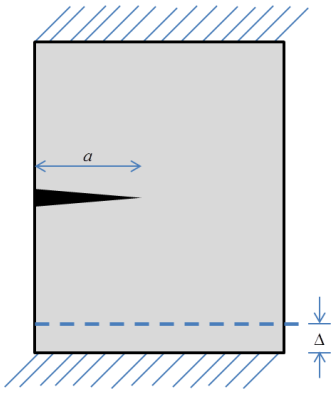

Figure 5.Cracked plate at fixed displacement

This case, $W = 0$ and $\Pi = U$ in which:

$$G = -\frac{1}{B}\left(\frac{dU}{da}\right)_{\Delta} = -\frac{\Delta}{2B}\left(\frac{dP}{da}\right)_{\Delta} \qquad (1.4.11)$$

Under displacement controlled conditions, the energy required for the crack extension is supplied by the strain energy in which decreases shown in Figure 6.[12]

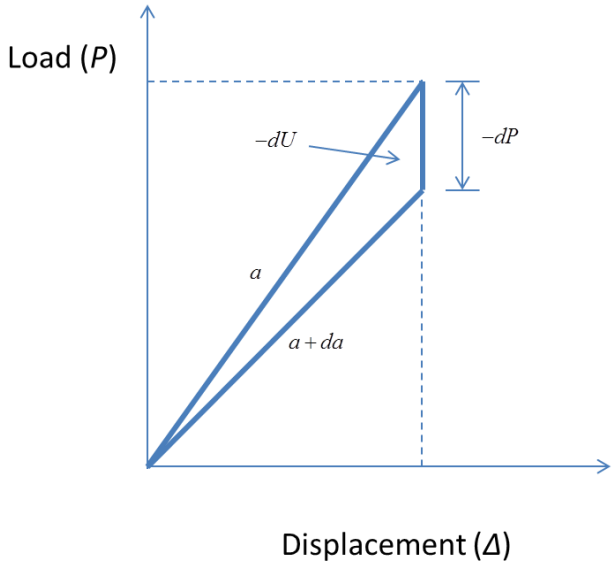

Figure 6.Graphical representation of displacement controlled test

From these both cases, compliance is introduced in which takes the form of:

$$C = \frac{\Delta}{P} \tag{1.4.12}$$

With the compliance substituted in both Eqn.(1.4.10) and Eqn.(1.4.11), the result for both load and displacement control comes out to be [12]:

$$G = \frac{P^2}{2B}\frac{dC}{da} \tag{1.4.13}$$

This concludes that the energy release rate from Eqn.(1.4.13) is the same for both load and displacement control in which:

$$\left(\frac{dU}{da}\right)_P = -\left(\frac{dU}{da}\right)_\Delta \tag{1.4.14}$$

With these both cases of the energy release rate, there is further analysis on the behavior of cracks. Two parameters that were discussed previously, the energy release rate and the stress intensity factor, have a relationship in which characterizes and quantifies the behavior of cracks. The energy release rate describes the behavior globally; the stress intensity factor describes the behavior locally [10]. As for this research which deals with linear elastic fracture mechanics, the stress intensity factor, *K*, and the energy release rate, *G* are distinctively related. In order to fully depict the correlation between the energy release rate *G* and the stress intensity factor *K*, combining Eqn.(1.4.2) and Eqn.(1.4.7) leads to the relationship between both parameters for plane stress:

$$G = \frac{K_I^2}{E} \tag{1.4.15}$$

and for plane strain,

$$G = \frac{K_I^2(1-\upsilon^2)}{E} \tag{1.4.16}$$

where these relationships are proved to be general and assumed that the energy release rate *G* associated with the advancement of crack Δa is linked to the work required to close the crack in a region according to:

$$G = \lim_{\Delta a \to 0}\left(\frac{\Delta U}{\Delta a}\right)_P \tag{1.4.17}$$

where ΔU is the work of the crack closure. Another method of measuring the energy release rate for linear and nonlinear elastic materials was proposed called the J-Integral.

1.4.4 J-Integral

The J integral is equal to the strain energy release rate for a crack in a body subjected to monotonic loading. This equivalence is considered true only for linear elastic materials that experience small scale yielding at the crack tip, the J can be utilized to compute the energy release rate under special circumstances such as monotonic loading.

The J-Integral, developed by Rice under small scale yielding conditions:

$$G = J = \int_c \left(wn_i - T_i \frac{du_i}{dx} \right) ds \tag{1.4.18}$$

where w is strain energy density:

$$w = \int_0^{\varepsilon} \sigma_{ij} d\varepsilon_{ij} \tag{1.4.19}$$

n_i is the normal vector to c, and T_i is the traction vector:

$$T_i = \sigma_{ij} n_j \tag{1.4.20}$$

c is an arbitrary contour around the tip of the crack; σ , ε, and u are the stress, strain, and displacement field, respectively [13]. Since this adhesion testing method deals with a narrow crack in the body of interest with a yielding zone small in size comparing to the dimensions of crack size and specimen width, small scale yielding conditions are considered. To further illustrate the elementary principles of the J-integral with its small scale yielding conditions, form of stresses are shown below in Figure 7.

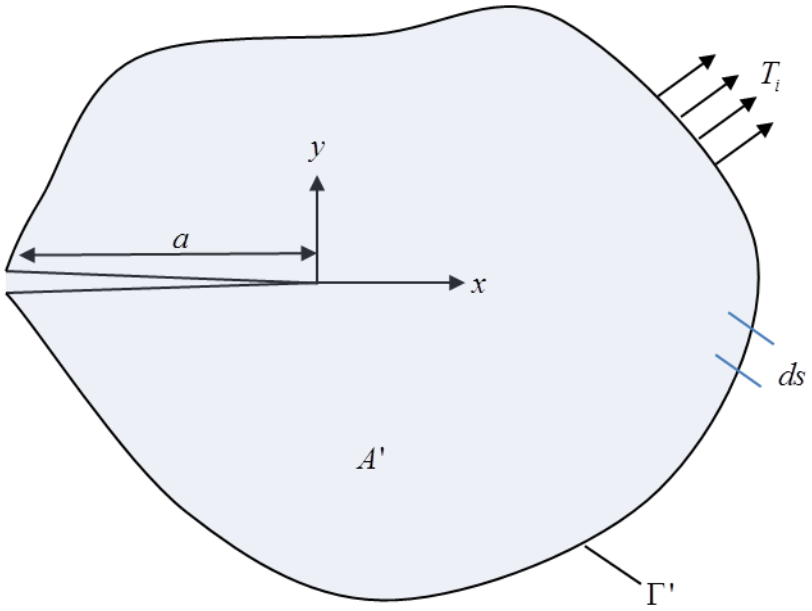

Figure 7. 2D body bounded by Γ

Let *A'* represent the area of the body shown above where the coordinate axis is on the crack tip. The potential energy, under quasistatic conditions, is given by [9]:

$$\Pi = \int_{A'} w dA - \int_{\Gamma''} T_i u_i ds \tag{1.4.21}$$

where *Γ''* is the segment of the contour where tractions are defined. With the change in potential energy resulting from an extension of the crack into consideration:

$$\frac{d\Pi}{da} = \int_{A'} \frac{dw}{da} dA - \int_{\Gamma'} T_i \frac{du_i}{da} ds \tag{1.4.22}$$

in which line integration is conducted for the whole contour *Γ'* since $\frac{du_i}{da} = 0$ at the region where displacements are specified. In addition, $\frac{dT_i}{da} = 0$ at the region where tractions are specified. Since the crack extends for an increment of *da*, the coordinate axis moves with respect to the crack extension in which can be expressed as:

$$\frac{d}{da} = \frac{\partial}{\partial a} + \frac{\partial x}{\partial a}\frac{\partial}{\partial x} = \frac{\partial}{\partial a} - \frac{\partial}{\partial x} \tag{1.4.23}$$

since $\frac{\partial x}{\partial a} = -1$. By using Eqn.(1.4.23) into Eqn.(1.4.22) shows:

$$\frac{d\Pi}{da} = \int_{A'}\left(\frac{\partial w}{\partial a} - \frac{\partial w}{\partial x}\right)dA - \int_{\Gamma'} T_i\left(\frac{\partial u_i}{\partial a} - \frac{\partial u_i}{\partial x}\right)ds \tag{1.4.24}$$

where $\frac{\partial w}{\partial x} = \frac{\partial w}{\partial \varepsilon_{ij}}\frac{\partial \varepsilon_{ij}}{\partial x} = \sigma_{ij}\frac{\partial \varepsilon_{ij}}{\partial x}$ in which comes from the strain energy density in Eqn.(1.4.19); with the addition of applying the strain-displacement relationship to the $\frac{\partial w}{\partial x}$ relation:

$$\frac{\partial w}{\partial x} = \frac{1}{2}\sigma_{ij}\left[\frac{\partial}{\partial x}\left(\frac{\partial u_i}{\partial x_j}\right) + \frac{\partial}{\partial x}\left(\frac{\partial u_j}{\partial x_i}\right)\right]$$

$$= \sigma_{ij}\frac{\partial}{\partial x_j}\left(\frac{\partial u_i}{\partial x}\right) \tag{1.4.25}$$

since $\sigma_{ij} = \sigma_{ji}$. Using this relationship into Eqn.(1.4.24),

$$\frac{\partial w}{\partial a} = \frac{\partial w}{\partial \varepsilon_{ij}}\frac{\partial \varepsilon_{ij}}{\partial w} = \sigma_{ij}\frac{\partial}{\partial x_j}\left(\frac{\partial u_i}{\partial a}\right) \tag{1.4.26}$$

in addition to applying the principle of virtual work (which is when a rigid body or system is in equilibrium, the derivative of its potential energy with respect to crack length extension is zero)the change in potential energy is shown as [9]:

$$\int_{A'}\sigma_{ij}\frac{\partial}{\partial x_j}\left(\frac{\partial u_i}{\partial a}\right)dA = \int_{\Gamma'} T_i\frac{\partial u_i}{\partial a}ds \tag{1.4.27}$$

This equation is then applied in the line integral in Eqn.(1.4.24) which results in the following:

$$\frac{d\Pi}{da} = \int_{\Gamma'} T_i \frac{\partial u_i}{\partial x} ds - \int_{A'} \frac{\partial w}{\partial x} dA \tag{1.4.28}$$

With the Divergence Theorem being applied as well as multiplying both sides of the equation above by -1, the energy release rate comes down to:

$$\begin{aligned} -\frac{d\Pi}{da} &= \int_{\Gamma'} \left(w n_x - T_i \frac{\partial u_i}{\partial x} \right) ds \\ &= \int_{\Gamma'} \left(w dy - T_i \frac{\partial u_i}{\partial x} ds \right) \end{aligned} \tag{1.4.29}$$

since $n_x ds = dy$ [9]. As a result for a linear elastic material, the J contour integral is equivalent to the energy release rate G which is in relation to the stress intensity factor K.

With this energy release rate definition, one can measure the adhesion strength within a solid and between two materials under different type of loading conditions in a variety of measurement methods.

1.5 *Overview of adhesion test methods for rigid/flexible/rigid multilayer systems*

1.5.1 Double cantilever beam

As one of the few adhesion testing methods being discussed, the double cantilever beam test is reviewed. This configuration utilizes tensile loading which refers back to Mode I loading in order to find the intrinsic adhesion strength. This configuration consists of a multilayer sandwich beam which is fabricated with end

supports for tensile testing. In addition, a pre-crack is made at the interface of interest as shown below in Figure 8:

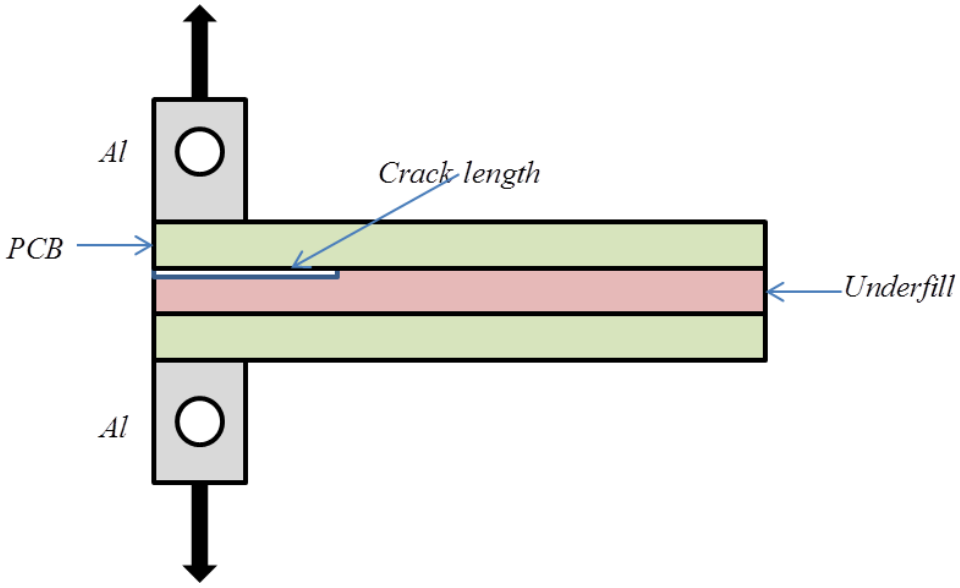

Figure 8.Double cantilever beam with PCB substrates and underfill

where two rectangular plates are cut from PCB substrates which are then sandwiched with the underfill in between them [14]. The pre-crack is shown in which is defined in the sandwiched area between the two PCB substrates and the underfill. The aluminum end blocks are used for the purpose of reinforcing the PCB beam during testing. So in order for the pre-defined crack to propagate, a mold release agent is used to from a weakly bonded area to create the initial delamination between the PCB substrate and the underfill.

As for the experiment, tensile loading is applied at a constant displacement rate in which a critical load and the compliance of the specimens are extracted from a load vs. displacement plot. Multiple tests can be run on one specimen to extract those parameters. However in order to not depend and require a crack length measurement

for the specimens, analytical solutions were applied so that the crack length can be predicted from the compliance and therefore extract the energy release rate from the critical load and crack length with decent precision [14].

The double cantilever beam method delivers minimum amount of plastic deformation due to the tensile or Mode I loading which makes the accessibility to the energy release rate easier. This method produces a controlled and stable growth of the interfacial crack of the specimens in addition to having established reproducible testing procedures [10]. In contrast to the advantages of this test, one must take laborious steps for these sample preparations which involve the adherend, accurate initial crack length, and fabrication of the overall beam. In order to prevent mode mixity, perfect tensile loading is required since unexpected in-plane shear loading or Mode II can unexpectedly affect the test results.

1.5.2 Four point bending with side cracks

In this adhesion testing method, the application of four point bending is used on typical flip-chip assemblies. This method is conducted mostly because of the importance of interfacial strength in which determines the reliability of typical flip-chip assemblies in electronic packaging [15-17]. In addition, the setup can test real packages under mixed loading conditions along with the advantage of containing the steady state adhesive region that exists between inner loading pins. Two specimens are set up by having layers of a silicon chip with passivation coating, underfill, and a circuit board along with two symmetric edge cracks at the interface of interest right in between the circuit board and the underfill. Shown below in both Figure 9 and Figure

10, the symmetric edge cracks are located differently for each specimen where one has the cracks at the interface between underfill and silicon chip in contrast to the other having the cracks at the interface between underfill and circuit board [17].

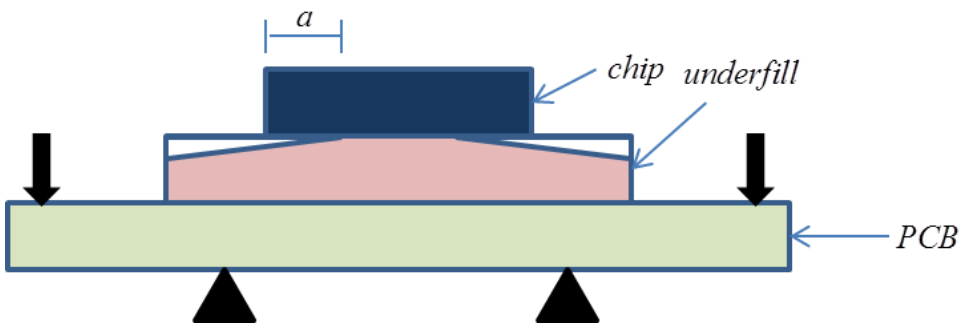

Figure 9.Side cracks between underfill and silicon chip

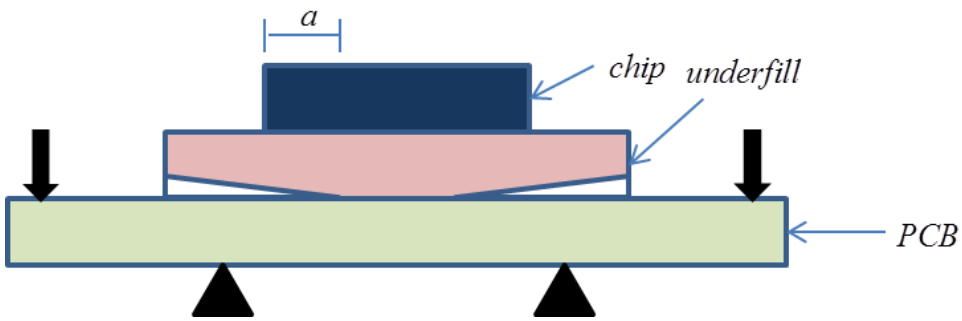

Figure 10.Side cracks between underfill and circuit board

where *a* is the crack length with two symmetric loads being applied onto the circuit board. In terms of specimen preparation, the initial interfacial crack is fabricated by spraying a mold release agent on the area of interest, either underfill/circuit board or underfill/silicon chip [17]. The underfill is utilized to be adhesive between the silicon chip and the circuit board.

The specimens are inserted into a four point fixture at displacement control in which a constant load point displacement rate was set. During testing, both specimens deform linearly with respect to the gradual increase of the bending moment. With this, the interfacial side cracks begin to propagate until a critical load has been reached. Respective to the critical load, P_c, a sudden load drop is present due to the reduced stiffness of the specimen [17].

The critical peak load, P_c, recorded is associated with the onset of crack growth in which is used to convert into interfacial toughness [17]. In addition, analysis solution for the energy release rate is derived so it can be utilized to attain toughness from critical loads. The analysis solution for the critical energy release rate, G_c, is evaluated by using the difference in strain energy stored in the cracked and uncracked beam since it is an indication of the adhesion strength of an interface. This is equal to the path independent J-integral which was used in order to define the critical energy release rate.

Following the evaluation of the J integral to get G_c , the critical energy release rate, for the specimen with the side cracks, the critical load, P_{crit}, from the four point bending experiment is utilized as an input into an Finite Element Analysis Model to determine the stress and displacement fields surrounding the crack tip. With this being established, the J-integral is extracted from the Finite Element Analysis Model results.

As for the advantages of conducting this type of adhesion testing method, testing real packages with flip chip assemblies in electronic packaging are plausible and viable to measure the interfacial toughness. During the evaluation of the

experimental results, the energy release rate is independent of crack length ($a>2h$). These testing procedures are established and reproducible for future testing on these types of packages with constant and unvarying boundary conditions [10]. Using the side crack method in selecting the components such as die passivation, solder mask, and underfill in the design phase can reduce the development cycle, time, and cost. In contrast to the advantages of this method, it is difficult to fabricate two symmetric side cracks even though release agent spray is used which cannot guarantee the exact identical dimensions for the cracks [10].

1.5.3 Four point bending with a vertical notch

Another configuration of an advanced adhesion test method is the four point bend test. A typical specimen for this type of test which determines the adhesion strength between layers in the sandwiched structure consists of a vertical notch which enables the horizontal pre crack, a, along the interface [18]. This four point bend test setup takes an advantage of the steady state adhesion region that occurs between the inner loading pins. As for the experimental procedure is concerned, this test is applied at a constant displacement rate which allows a steady crack to propagate. During the experiment, a peak load is reached which means that the crack of the specimen begins to propagate stably along the interfacial layer of interest. There are two types of failure modes for this four point bend test: clear delamination of the coating from the substrate, and delamination followed by substrate cracking [10].

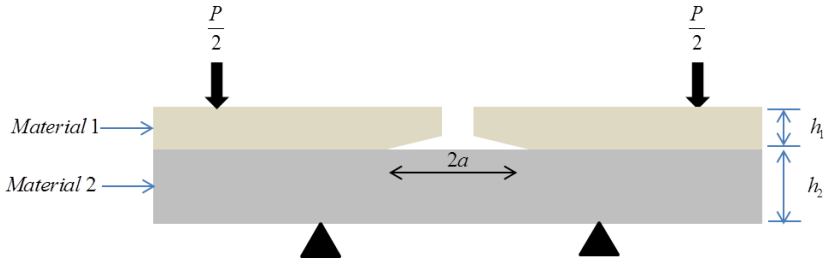

Figure 11. Bimaterial beam with vertical notch

The accurate depth of penetration of the failure mode is determined by the elastic properties of the substrate as well as the coating. Extending from the basic configuration of the four point bend test, one common setup of a specimen is a stack of using two dissimilar layers with a pre crack at the interface. As for testing a bimaterial beam from Charalambides, a four point bend test measures the fracture resistance of these types of interfaces as shown above in Figure 11 [19-21]. According to Charalambides, the energy release rate or adhesion strength is independent of the debond length when the interfacial crack extends sufficiently far from the vertical pre-crack [19]. In agreement to Charalambides, Dauskardt took off from this methodology by sandwiching a thin multilayer stack between two enormous elastic substrates in order to solve for the energy release rate as shown below in Figure 12 [22]:

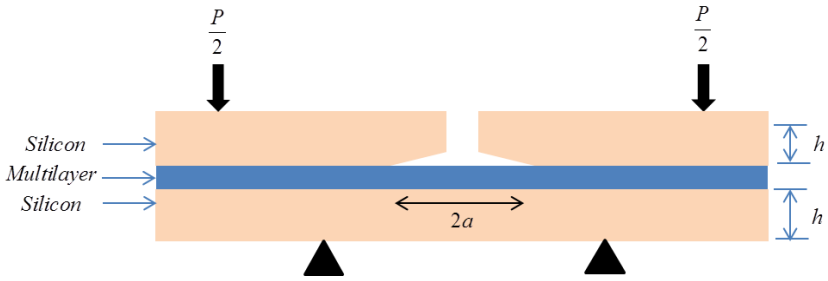

Figure 12. Multilayer stack between similar substrates with vertical notch

Along with how this four point bend test can achieve in getting the adhesion strength from the critical load under a constant displacement rate, this test has its own advantages and disadvantages which enable researchers to decide which adhesion testing method gives out the most full quantitative information on the adhesion strength of the coatings/epoxies. This is taking advantage of the simple beam mechanics involved in this problem [10]. This four point bend test can determine the steady state adhesion strength which is independent of crack length. Specimens can be easily fabricated and be easily reproduced under variety of conditions as well as converting load-displacement data into fracture toughness results. This type of results or data allows the user to predict failure modes of different type of structures based on material properties, loading conditions, and geometry [10]. In contrast to the advantages of this test, mixed mode loading conditions are introduced due to the nature of the four point bending test. In addition, this test is only suitable for analysis from a limited pool of specimen geometries going from small scale to a really large scale. As for manufactured parts, the four point bend test is questioned to see if this can sufficiently simulate the stress/strain loading environment which those

1.6 *Motivation of work*

Delamination occurring in a variety of structures within today's microelectronic packaging plays a dominant reliability role in the industry. A necessity for measuring adhesion strength in relation to finite element modeling analysis is essential to solving problems for multilayer structures. For evaluating thin film mechanical properties and behavior, the four point bending test has been one of

the popular methods in which can take advantage of the steady state *G* region that is independent of crack length compared to other tests discussed previously. For testing those very thin samples such as an EMC/PSR/PCB configuration, low fracture toughness induces kinking beyond the interface of interest. Due to this dilemma, there is a need for a pre-defined area to avoid this problem. By using the four point bending test which was used by works done by Evans, Dauskardt, and Suo, an opportunity arises to determine the critical energy release rate of practical multilayer structures that cannot be considered "essentially bi-material systems" or under plane strain conditions.

1.7 *Objective of work*

The objective of this work is to extend the work of previous four point bending test studies on the application of adhesion strength in a multilayer structure by investigating and understanding the crack front behavior visually and analytically. The crack front behavior in a multilayer system under four point bending is then correlated to the load-displacement profile under non plane strain conditions with the aid of transparent substrates. To fully evaluate the nature of the interfacial fracture toughness of this study's multilayer system, a 3D finite element model is fabricated to compute the adhesion strength along the crack front. This work also drives another goal to fabricate a reproducible and effective procedure to utilize a concept of a pre-defined area to create successful pre-cracks before testing. This enables to eliminate load overshoot when the specimen undergoes compressive loading. Consistent sample preparation involving the pre-defined area aims to reduce scatter in adhesion strength data sets. With the reduced scatter in the results at a room temperature setting, one

can reproduce the same multilayer specimens to conduct environmental degradation such as moisture. With a reproducible four point bend testing protocol and sample preparation, the guidelines set by the investigation of the crack front due to transparent specimens can be used for real packages to avoid kinking and obtain consistent results with the help of a pre-defined area.

CHAPTER 2: MULTILAYER ADHESION TEST

2.1 *Overview of rigid/flexible/rigid 4PB test with a vertical notch*

Previously, different methods exist to analytically characterize the mechanical behavior of interfaces which consist of thin film substrate configurations as well as bi material cases. Different fracture behaviors at various focused interfaces under a variety of load conditions have been analyzed. The effort made by Charalambides and Dauskardt offers the opportunity to determine the critical adhesion strength or the energy release rate by means of four point bending. However these methods assume bimaterial or essentially bimaterial cases that does not take into consideration of a third thin layer sandwiched between. This thus allows one to advance with experiments to extend bimaterial cases to simple multilayer rigid substrate cases. The sample configuration under four point bending of this research is shown below:

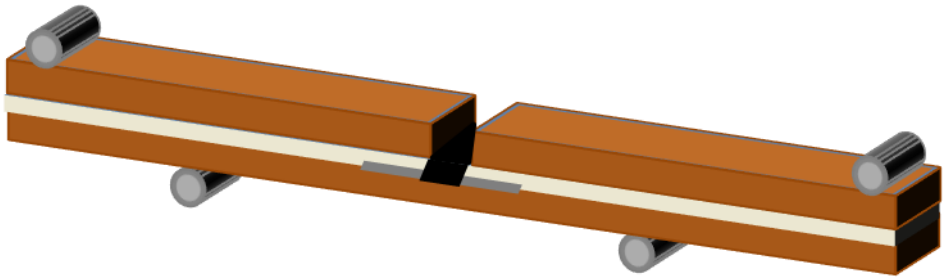

Figure 13. Schematic of a bronze multilayer specimen under four point bending

where two rigid bronze substrates as the adherends, an adhesive epoxy layer as the middle layer, and a pre-defined area composed of silicon oil and aluminum deposition with a vertical notch that allows the opening of the pre-crack. For this type of adhesion test, specimens are easily reproducible under the same variety of conditions

in which geometric and mechanical parameters, displacement rate control, sample pre-crack are crucial for this experiment. A system of having consistent reproducible specimens will be introduced along with discussing the modifications of previous literature studies and challenges in which leads up to verification and extension of Charalambides' and Dauskardt's work.

2.1.1 Steady state region

In order to fully understand what Charalambides and Dauskardt have done to tackle the fracture mechanics problem of sandwiched bimaterial and thin film structures, the concept of the steady state region needs to be focused upon. The steady state region refers to a region where a crack is located between the inner loading pins or points under constant bending moment, M_b, which causes the strain energy release rate to display steady state characteristics shown below [22]:

$$M_b = \frac{P\ell}{2b} \tag{2.1.1}$$

where *P,l,b* represent the applied force, pin spacing, and the sample width respectively. Graphically in a load vs. displacement diagram, the steady state region can be depicted as follows:

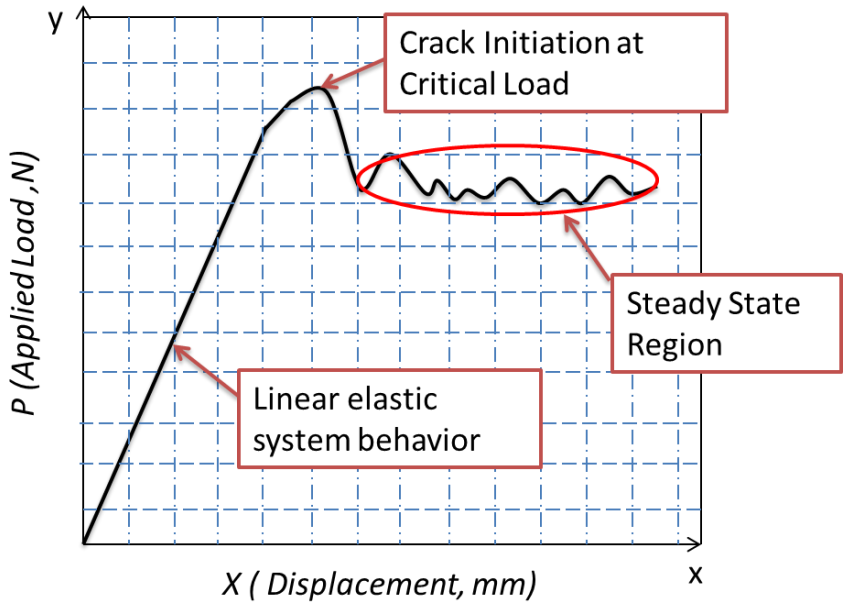

Figure 14.Typical load vs. displacement curve of four point bend test

The steady state strain energy release rate is also achieved when the interface crack length significantly exceeds the thickness of the overall thickness of the delaminating system of a sandwiched beam which is the top substrate and the adhesive layer.

2.1.2 Pre-defined area

As a requirement for measuring the crack extension driving force or energy of an interface of interest, a pre-crack must be established on both ends of a pre-defined area. The pre-defined area's sole purpose is to act as a release agent in which a pre-crack for the multilayer specimen can be introduced. A vertical notch, in the middle of a multilayer specimen, plays a part which allows an opening for the pre-crack to occur. The pre-defined area of a specimen for this research is composed of two layers: silicon rubber oil and deposited aluminum. In order to guarantee that a pre-crack is

formed from this pre-defined area, acrylic multilayer specimens have been produced and tested for verification. Due to the transparent clear crack front of the acrylic specimens, it was proven that a pre-crack was able to be introduced from the pre-defined area configuration. Thus, the pre-defined area configuration was then passed onto the bronze multilayer specimens for further testing.

2.1.3 Numerical method for calculating *G*

From the Euler-Bernoulli beam theory and under the assumption of Hook's law, the steady state energy release rate, G_{ss}, is seen as:

$$G_{ss} = \frac{M^2(1-\nu_2^2)}{2E_2}\left(\frac{1}{I_2} - \frac{\lambda}{I_c}\right) \tag{2.1.2}$$

where

$$\lambda = \frac{E_2(1-\nu_1^2)}{E_1(1-\nu_2^2)} \tag{2.1.3}$$

with E and ν representing the elastic modulus and Poisson's ratio, and subscripts 1 and 2 referring to the top and bottom substrate where subscript c refers to the overall composite beam [22]. In this research case, λ is 1 since both the modulus and the Poisson's ratios are the same. The moments of inertia of I_2 and I_c are calculated as followed:

$$I_2 = \frac{h_2^3}{12} \tag{2.1.4}$$

and

$$I_c = \frac{h_1^3}{12} + \frac{\lambda h_2^3}{12} + \frac{\lambda h_1 h_2 \left(h_1 + h_2\right)^2}{4\left(h_1 + \lambda h_2\right)} \tag{2.1.5}$$

where the parameter *h* represents the substrates' thickness.

2.2 *Detail of experimental equipment*

For this research, a single column testing system, the Instron 5942, was used. This testing frame is capable of providing variable mode mixity for the application of fracture mechanics on different type of specimen configurations. To conduct four-point bending, two pin fixtures were fabricated, top and bottom, and fixed onto a testing platform and the loading cell. A full schematic of the experimental setup is shown below:

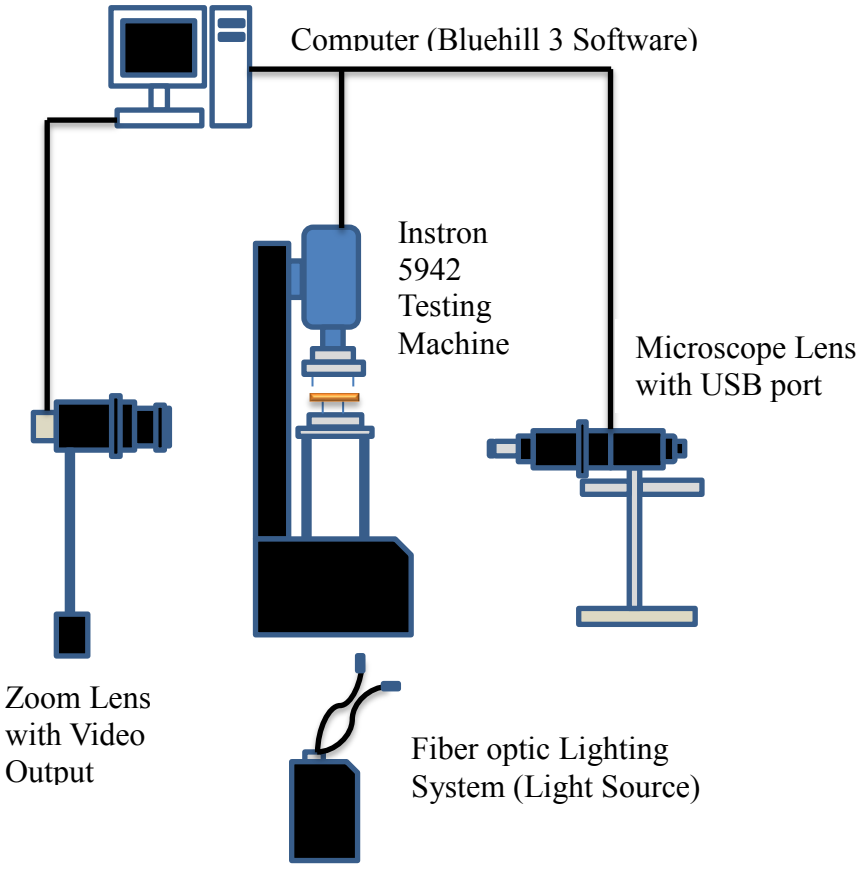

Figure 15. Schematic illustration of the experimental setup

2.2.1 Vacuum chamber

The Denton DV-502A vacuum chamber is utilized for the bronze specimens in terms of creating the pre-defined area with aluminum deposition. The chamber is an evaporator in which uses diffusion pump design. In addition, the DV-502A allows the user to evaporate materials that are commonly used in electron microscope specimen preparation such as carbon, platinum, and others like aluminum. The deposition procedure is conducted with a step-by-step manual in which results in having the silicon oil pre-defined area deposited with evaporated aluminum. The Denton DV-502A vacuum chamber is shown below:

Figure 16.Denton DV-502A vacuum chamber

2.2.2 Instron test stand

The Instron 5942 Single Column Testing System (Instron®) is one of the major components for this experimental setup. This system has an electromechanical load frame which is purely designed for tension, compression, and other stress testing. The load frame gives the user the required speed, position, and stiffness during testing. In addition to the load frame, a control panel is mounted that provides functions that allow the user to control the gauge length, load, and start/stop operations for the system. The control panel is mainly used to control crosshead movement during experiments such as the four point bending test when specimens are loaded and unloaded. In order to connect all the elements of the Instron system, control electronics are placed within the system which is attached to the load frame which includes the load conditioner board and the digital signal processor board. In terms of specifications, this system has a load measurement accuracy of ±0.5%, a speed range of 0.05 – 2500 mm/min, and a load capacity of 0.5 kN. These specifications are taken into advantage in which helps with testing these four point bending specimens.

(a)

Figure 17.(a) Instron testing stand and (b) Instron control module

The main control of the Instron 5942 is packaged with testing software, Bluehill 3 which controls the Instron testing systems for test control, setup, data collection, result generation, and report planning. For this research, it is essential to collect accurate data in which derives from graphs, result tables, and generated reports. Since a four-point bending test is classified as a compression test, the software is able to generate results based on the compression test profile which is configured by the user. The main data parameters that are mainly focused on from this four-point bend test are load and displacement (extension). The user is able to conduct multiple tests reproducibly in which the software is aware of what specimen parameters are inputted into the system. The pre-crack fatigue loading profile and the main test profile are created in this software for testing. The user interface of the Bluehill 3 software is depicted below:

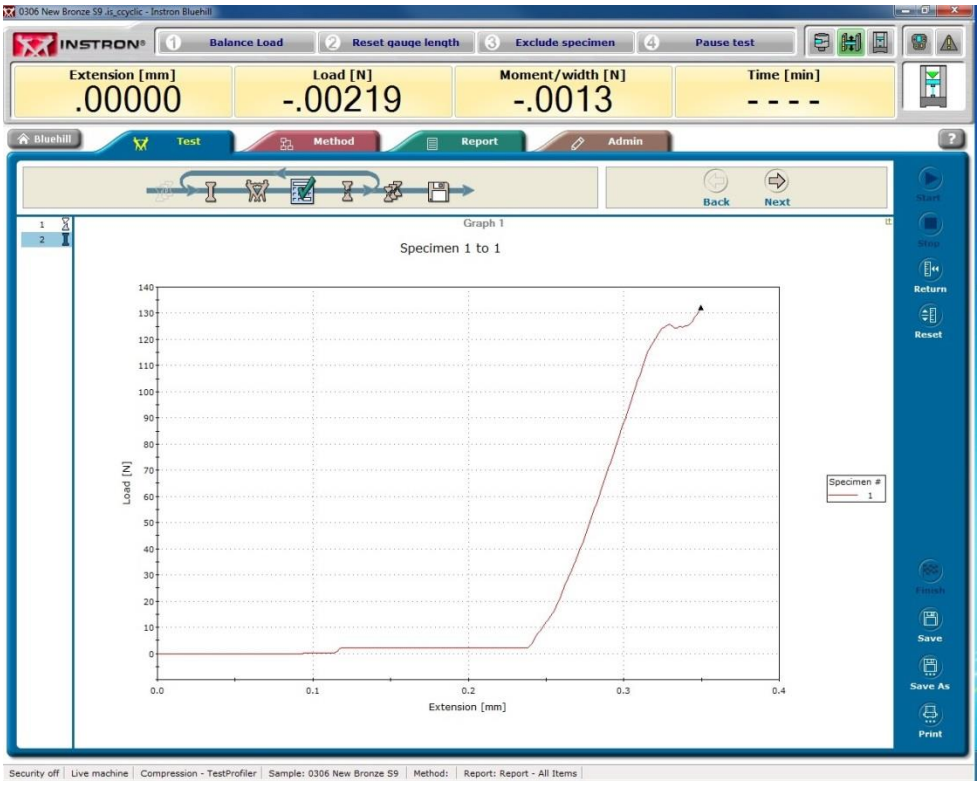

Figure 18. Bluehill experiment interface

2.2.3 4PB test fixture

In order to conduct a pure four-point bend test, top and bottom pin fixtures are fabricated and attached into the loading cell and onto the testing platform. The pin spacing between the top and bottom pins are configured for consistent testing of the specimens. The top pin fixture has a span of 70 mm whereas the bottom pin fixture has a span of 40 mm. The Instron 5942 with four-point bending pin fixtures is portrayed below:

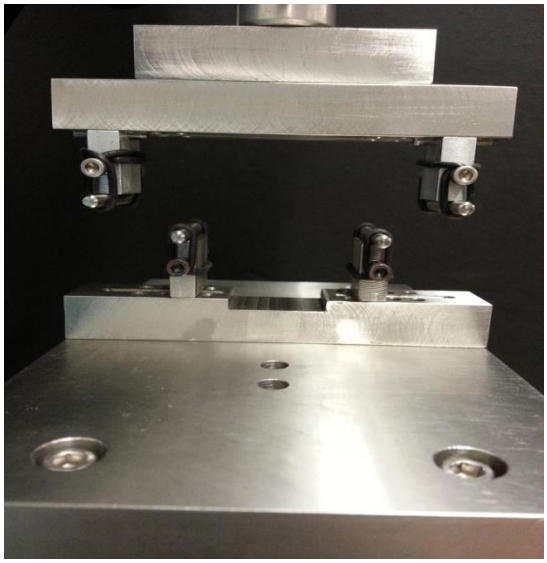

Figure 19. Four point bending fixtures

2.2.4 Photo & video capturing cameras

The two cameras that are used for this experimental setup are the Zoom Lens (18-108 mm F2.5) with a Sentech Video Module and the Mitutoyo Lens supported by a Navitar 1-6010 camera stand attached with a Sentech USB camera module. The zoom lens is used for video recording the pre-crack of the pre-defined area with the assist of a right angle mirror prism placed underneath the specimen. The crack front is portrayed by the mirror prism in which the user can observe the initial crack depicted on the computer screen. However this was only used for the Acrylic specimens due to its transparency of the substrates. For the bronze specimens, the zoom lens for video recording was not needed since the crack front cannot be observed. As for the other camera, the Mitutoyo camera lens mounted with the camera stand is used for capturing up-close snapshots of the edge of the specimens to portray the delamination or crack propagation. The cameras are shown below in Figure 20 and Figure 21 :

Figure 20. Zooms lens with video module

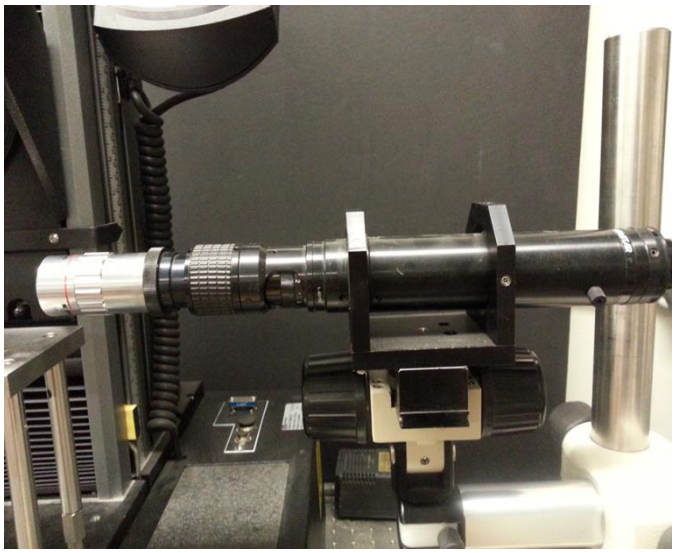

Figure 21. Mitutoyo lens with USB camera module

2.2.5 Fiber optic light source

In order to capture and visualize the specimen's crack behavior, the FSI 1060-150 Fiber Optic Light Source is used. This light source contains a 150 Watt quartz halogen lamp which utilizes an integrated dichroic reflector that focuses the maximum light intensity into the fiber optic ring lights. The ring lights are positioned in a way that the light can focus just mainly on the area of interest where both ends of the crack are present. The light source is portrayed below in Figure 22:

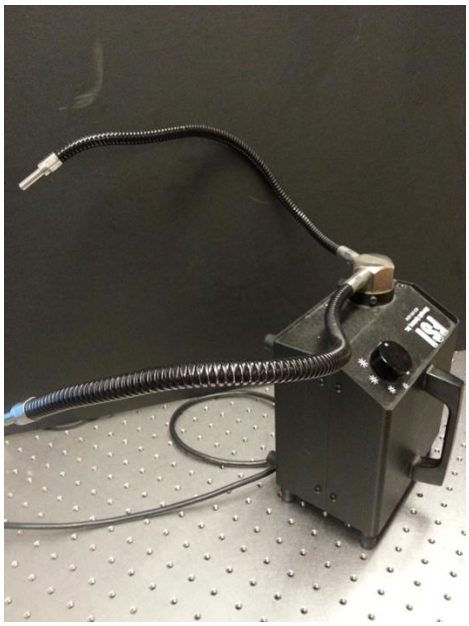

Figure 22. Fiber optic light source

2.3 *Experimental procedure*

2.3.1 Specimen preparation for multilayer specimen

Each specimen will consist of three parts: one bottom substrate, one adhesive layer, and two top substrate pieces, which allow a vertical gap of 2 mm in the pre-

defined area. The purpose of having two pieces of the top substrate rather than one whole top substrate is to eliminate the need of milling the vertical notch for the opening of the pre-crack. This will prevent residual stresses after milling due to immense vibration which can cause unwanted delamination along the crack front. Both acrylic and bronze specimens are made according to this sample procedure. However for this explanation of the main sample procedure, fabrication of bronze specimens is specified.

The bottom substrates and top substrates are cut to its approximate length of 75 mm and 36.5 mm, respectively both with widths of 12.7 mm by assistance from the services of the campus' machine shop. The thickness of the substrates is 3.175 mm, uniform all across the substrates which helps achieve evenly distributed adhesion. The surfaces of the cut substrates are then roughened up uniformly with GRIT 240 sandpaper in order to create metal interlocking that enhance adhesion between the adhesive and the substrate [7].

The substrates are then to be cleaned with water and soap thoroughly to prevent unwanted contaminants such as oils to degrade the adhesion. Once they are dried up to avoid moisture, the edges of the substrates are taped with Kapton tape in order to prevent epoxy leakage when the layers are sandwiched during curing shown below in Figure 23:

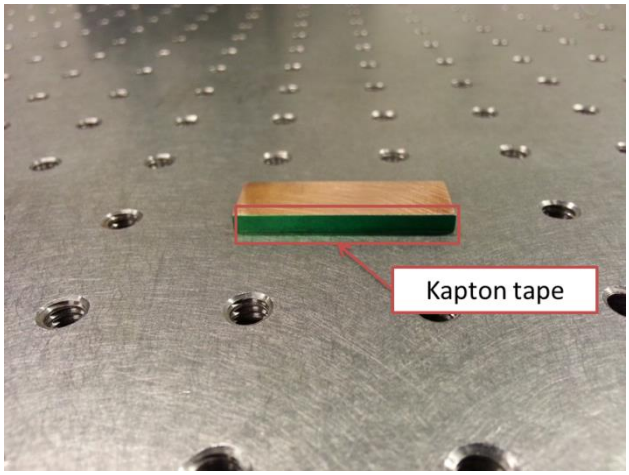

Figure 23. Tape covering the sides of the substrate

2.3.2 Creating predefined area

Following the cutting and cleaning of the substrates, the 75 mm substrates are selected for aluminum deposition within the area of applied silicon rubber. The silicon rubber and metal deposition procedure is conducted to fabricate a pre-defined area that acts as a release agent for the initial crack of the experiment. The reason silicon rubber oil was used is because of its high purity and quality which involves not having adhesive promoters that induces high surface tension. This allows the silicon rubber to have low adhesion on a surface.

Each bottom substrate will have a metal deposited pre-defined area of 127 mm^2 including the silicon rubber oil covering the deposited area. In order to achieve the pre-defined area of interest with no leakage from the applied silicon rubber oil, the top surfaces of the substrates are covered with scotch tape.

The bottom substrates are put under a top cover framing layer which has a middle rectangular through-hole having a width of 10 mm. This top cover is used as a

guideline for the pre-defined area in which an exacto knife is used to cut the scotch tape along the edges of the through-hole that defines the area of interest. The top cover is taken off of each bottom substrate so that the cut area of scotch tape can be peeled off, leaving the pre-defined area uncovered. Once the bottom substrates' pre-defined area has been uncovered, a small drop of the silicon rubber (RTV615A) is placed onto a flat metal working plate.

Figure 24. Silicon rubber deposition

A cotton swab is then used to dip and take some silicon rubber oil brushing across a pre-defined area of a bottom substrate until the pre-defined area is covered completely. Once all the bottom substrates' pre-defined area is covered with a thin layer of silicon rubber, a waiting time of 5 min is used in order for the silicon rubber to settle down.

Since the pre-defined area of the bottom substrates is covered completely with silicon rubber, they are then put into a vacuum chamber to complete the aluminum

deposition. The aluminum will come from a 0.01” diameter of a 1.5 foot long aluminum wire which is cleaned out with acetone to prevent unwanted residue such as oil and grease to be deposited onto the pre-defined area. The aluminum wire is then crumpled up into a ball so it can fit in the basket inside the vacuum chamber where evaporation takes place once the aluminum ball melts. With the procedures followed from the vacuum chamber manual in the lab, aluminum deposition on the pre-defined area of the bottom substrates is established shown in Figure 25, Figure 26, and Figure 27.

Figure 25. Aluminum deposition in vacuum chamber

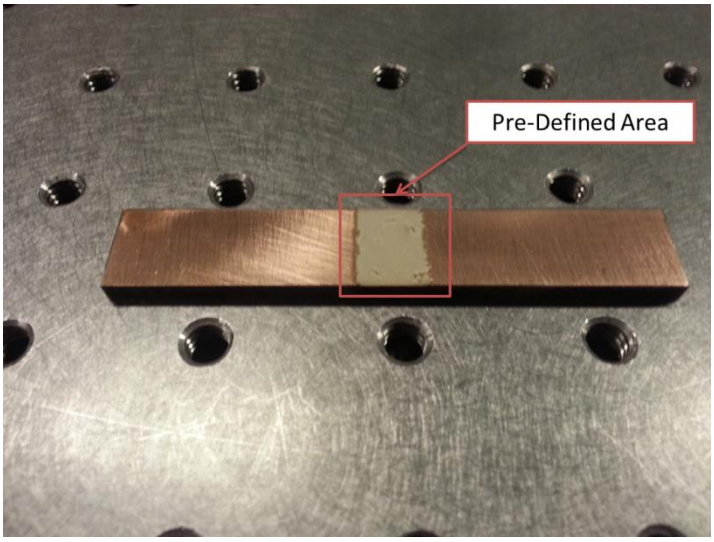

Figure 26. Pre-defined area of bronze bottom substrate

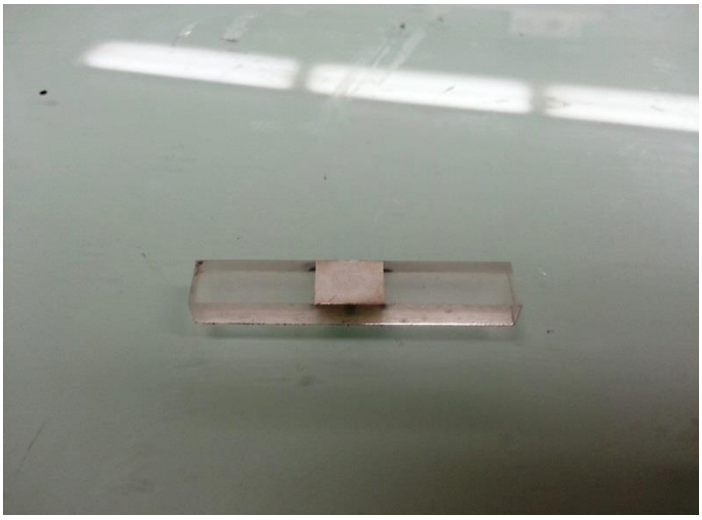

Figure 27. Pre-defined area of acrylic bottom substrate

2.3.3 Creating sandwich specimen

The adhesive for the specimens, Tra-Bond F114 epoxy, is then put into a mixing tube in which will be applied onto the bottom substrates after they have been deposited with aluminum by the vacuum chamber. The low viscous Tra-Bond F114 is composed of two parts: resin and hardener. Tra-Bond F114 is used for this specimen

prep due its popular usage in microelectronic packages. The Tra-Bond F114 epoxy package is displayed below in Figure 28:

Figure 28. Tra-Bond F114 epoxy

The required amount of epoxy should be calculated by how much resin and hardener one must use in order to cure the specimens. According to the datasheet of the Tra-Bond F114, the resin/hardener distribution for mixing is 100% weight of resin and 50% weight of hardener. Few drops of black dye are inserted into the tube for mixing. The purpose of the black dye is to properly see the adhesive, originally optically clear, during sample preparation and during testing. A spatula is needed to mix the adhesive thoroughly to prevent air bubbles forming and also making sure both the resin and hardener is mixed. In order to remove the bubbles trapped in the adhesive, the test tube is placed in the centrifuge container to have it spun for 2 min shown below in Figure 29:

Figure 29. Centrifuge for mixing epoxy

To complete and sandwich the final specimen, each bottom substrate is placed on the working table between two U-channel supports on the sides. These U-channel supports' purpose is to align the specimen on both bottom and top when sandwiched and cured.

The pair of top substrate pieces for each bottom substrate is then placed in which should be done in a slow cautious manner. Each top piece needs to start on one side slowly and place the other one down as well. This will prevent any trapping of air bubbles in the adhesive layer. If any epoxy leaks out, a cotton swab will be needed to gently remove the excess epoxy on the sides. Once this step has been established, slight adjustments need to be made just in case the substrates do not match up. The

specimens are then ready for curing for 48 hours at room temperature shown below in Figure 30.

Figure 30. Final curing step of specimen

2.4 *Fatigue testing for predefined crack propagation*

Fabricating the initial crack is also part of sample preparation. The purpose of this research is to analyze the behavior of cracked bodies or bodies with an initial crack. As stated previously, the pre-crack verification and crack front behavior investigation was conducted on Acrylic samples due to their crack front transparency. In order to fabricate the initial crack on the specimens, four-point bending with fatigue loading is used to initiate crack delamination within the pre-defined area.

The four-point bending with fatigue loading is conducted in a way where load is applied within an interval at a number of loading cycles. The displacement rate is constant for this setup which was taken at 5 mm/min to obtain initial crack opening.

The displacement rate was determined by a number of tests of bronze specimens that was best suitable for initial crack delamination. The fatigue loading cycle starts from a loading of 5 N all the way up to 10 N for ensured initial crack delamination. Previously in verifying the pre-crack initiation of the Acrylic specimens that were made, two cameras, each focusing on one side of the interfacial crack of the specimen, were used. One camera was used to portray a clear picture of the crack front with the help of a right angle prism mirror placed underneath the specimen, while the other camera is focused on the interfacial crack on the side. Since the bronze specimens are experimented upon, only the Mitutoyo lens with the USB camera module was used to capture the up-close images of the crack delamination.

2.5 *Monotonic testing for critical load*

To complement the fatigue loading profile discussed previously for the bronze specimens, the main full testing profile is conducted to test the specimens with four point bending. The displacement rate of the test run is set at 0.5 mm/min in order to fully grasp the stead state crack propagation when the specimen hits its critical load. In addition, the load cell of the main Instron 5942 must be balanced and calibrated due to the weight of the top pin fixture. The testing profile starts at ramping up to a set 3 N at the constant displacement rate in which the load is more than the top pin fixture. Due to this loading, one can accurately read the compliance of the specimen.

A criteria has been made in which determines the end of the test which is determined by a critical load drop, compliance change, end displacement of 2 mm, or the load cell reaches 475 N. The test is manually stopped after crack propagation.

2.6 *Post processing and analysis of results*

After conducting the four point bending test to all of the bronze specimens, critical load data were retrieved in order to determine the energy release rate through a J-integral calculation by numerical analysis.

CHAPTER 3: NUMERICAL ANALYSIS

3.1 *Finite element analysis of proposed technique*

In order to fully evaluate the adhesion strength or the J integral of the specimen configuration, a Finite Element Analysis was conducted. This numerical approach is utilized to determine the interfacial energy release rate for cracks that lie between two materials in multilayer structures. In addition, the FEA gives intuition on the overall design of the four point bending test which includes the sensitivity of the critical geometric parameters and sensitivity of mesh size and the J-integral value.

3.2 *Overview of 3D plane model*

Three dimensional linear elastic finite element analysis was performed by using the ANSYS 14 code. Both the geometry and the mesh utilized are shown below in Figure 31:

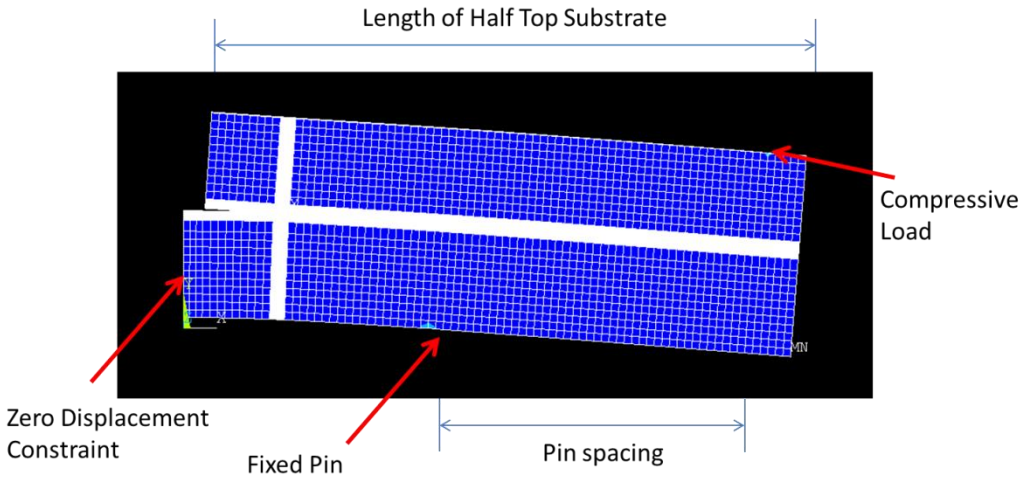

Figure 31. 3-D multilayer model

The finite element mesh consisted of eight nodes plane strain with quadrilateral elements type (PLANE183). Each element, which has translations in the nodal x, y, and z directions, was used as a plane element consisting of plasticity, stress stiffening, large deflection, and large strain capabilities. Due to the symmetric configuration of the multilayer beam, only one 3D quarter model was analyzed. The bottom half of the quarter model at one end is constrained at both x and y direction in which a single load is subjected at the other end of the beam with a bottom pin fixture. The adhesive layer of the quarter model was considered as another solid layer just as how the top and bottom substrates were fabricated. The thicknesses of the top and bottom substrate along with the thickness of the adhesive layer were used. Other physical parameters such as the elastic modulus and Poisson's ratio were taken into account for the bronze, acrylic, and the Tra-Bond F114 layers.

3.3 *Calculating J-integral in 3D*

As for numerically analyzing the energy release rate of the crack tip field, the J-integral calculation is used. The numerically stable J-integral solution can be calculated and evaluated along a contour surrounding the crack tip. This method has its advantages in which the contour integral can be applied to both linear and non-linear problems. In addition, the path-independence allows the user to evaluate J at a distant contour, which greatly increases numerical accuracy. The general J-integral model expression that is utilized for a 3D model case is again shown below:

$$G = J = \int_c \left(wn_i - T_i \frac{du_i}{dx} \right) ds \tag{3.2.1}$$

When calculating the J-integral of the 3D finite element model, a contour path of nodes is required and selected around the crack tip of the system. A rectangular path for this model is used to calculate the J-integral shown below in Figure 32.

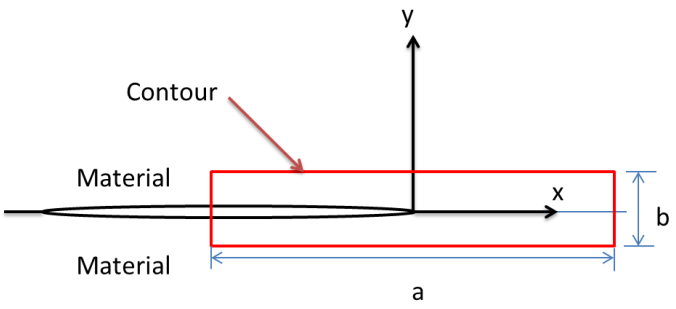

Figure 32. Rectangular contour path

This rectangular path consists of a short side length through the thickness, *b*, and a long side length, *a*, which can also be defined as $a = 10b$. The short side length, b, needs to be at least three elements away from crack tip to reduce numerical inaccuracy in the model [23]. As for the J-integral output from the FEA model, the J-integral value in terms of the z plane is plotted through the thickness. The maximum J-value can be determined at the center of the crack front, in addition to determining the percent deviation of J-integral values across the thickness from the maximum value. The 3D J-integral model after analysis of an acrylic specimen is shown below in Figure 33.

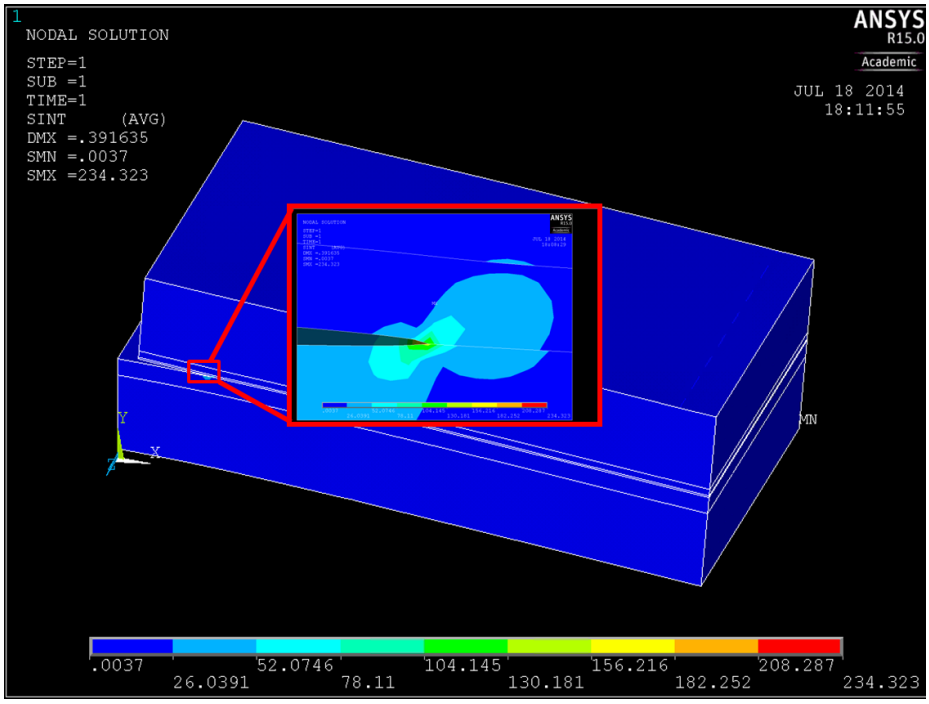

Figure 33. J-integral FEA model

3.3.1 Path independence

A significant characteristic of the J-integral when it comes down to evaluation of the crack tip is that the integral is path independent. For contours, as long there are no singularities existing between them, the J-integrals along the contours are identical or path independent. As for cases is concerned, the J-integral path independence evaluation of a homogeneous or bimaterial configuration can be extended to a multilayer case as long as there is only one singularity within the contour, each layer being a homogeneous elastic layer, and each layer remaining parallel to one another along with the crack.

3.4 *Mesh sensitivity study & J-Integral sensitivity study*

To fully grasp the numerical analysis of the J-Integral with less scatter in the values, a mesh sensitivity study was needed. This study enables one to pinpoint the adhesion strength value with the flexibility of being able to utilize different mesh sizes for a model. With this 3D quarter-model of the multilayer beam, parameters for near crack tip mesh as well as through thickness element ratio are factors in assuring mesh sensitivity. The predicted energy release rate is stated to be close to a stable value if the *b/a* ratio of the rectangular contour path of less than 0.1 is utilized. Combinations of different layers of elements are used for this mesh sensitivity in relation to the J-integral values as shown below in Table 1.

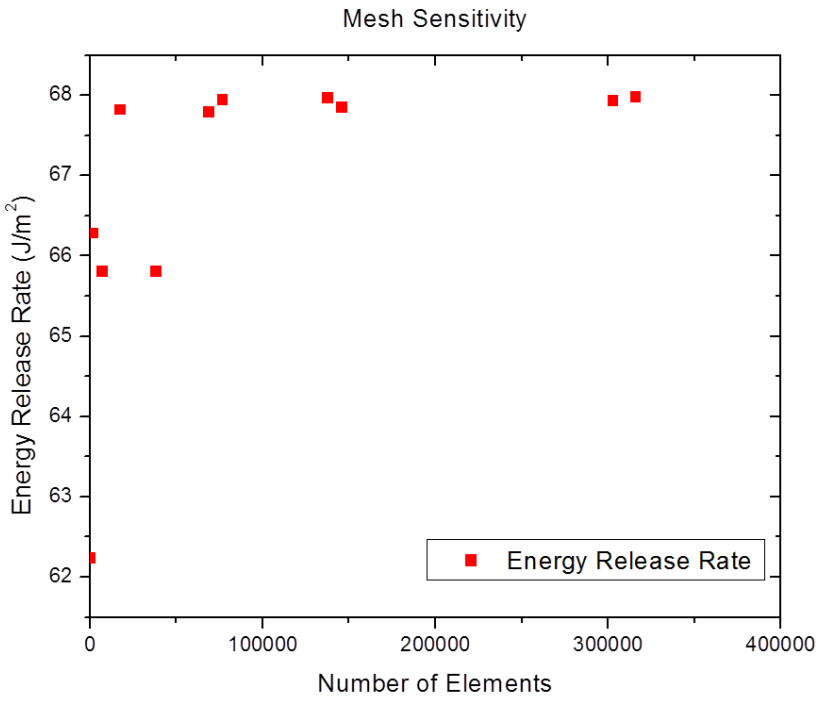

Figure 34. Mesh sensitivity in relation to J-integral (Energy Release Rate)

100 um center thickness					
Case	elm_thick	z_ratio	width elms	num_elms	J-Integral Values
1	1	50	0.8	179	62.23
2	2	50	1.6	1384	66.28
3	3	50	2.4	7028	65.81
4	5	50	4	38340	65.81
5	6	50	4.8	68775	67.79
6	8	50	6.4	145842	67.85
7	10	50	8	302744	67.93
8	3	25	4.8	17570	67.82
9	5	25	8	76680	67.94
10	6	25	9.6	137550	67.96
11	8	25	12.8	315991	67.98

Table 1. Mesh Sensitivity Table of J-Values

Based off of these results from the mesh sensitivity study, the recommended mesh for this 3D FEM model uses an element thickness of 5, through thickness element ratio of 25 with an element width of 8.

Along with the mesh sensitivity, the J-integral computation itself needs to undergo a sensitivity study where evaluating the J-values along several different contour paths are determined. As stated previously, in order to calculate a path independent J-integral, requirements of having at least three elements between the contour and the crack tip as well as having a ratio of long to short side greater than 10 yields stable results [23]. The sensitivity study involving three different *ab* ratios for the J-integral is shown below in Figure 35:

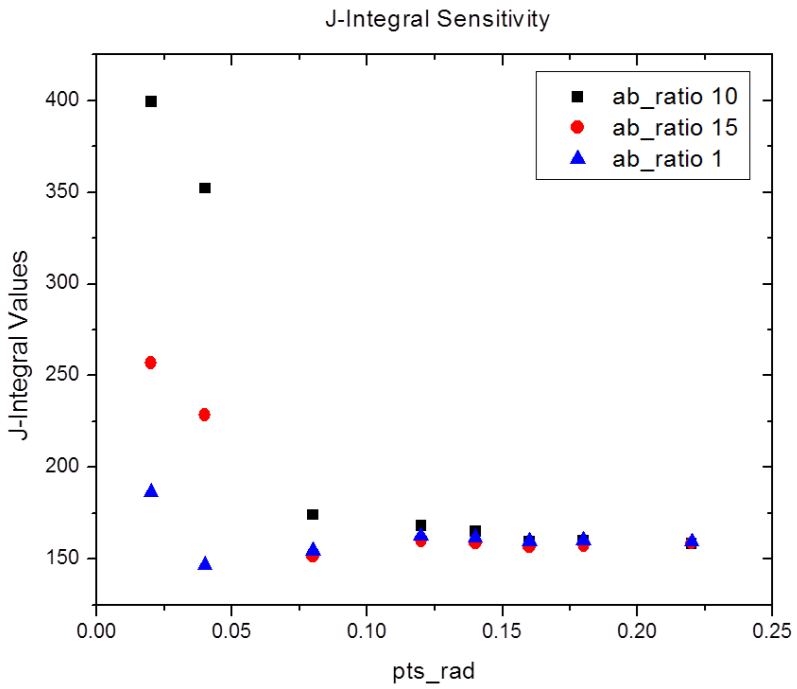

Figure 35. J-integral sensitivity

In accordance with the recommendations from authors regarding this J-integral numerical method, the following parameters of the *ab* ratio of 10 and the *pts_rad* calculated to be 1.8 times the thickness of the adhesive are required.

CHAPTER 4: EXPERIMENTAL RESULTS

4.1 *Investigation of crack front*

Before the bronze multilayer specimens are put into experiment, investigating the crack front behavior is essential to know in order to correlate with the load-displacement profile. The assumption is made where the specimens are tested under non plane strain conditions since it is not practical to test very wide specimens with the four point bending test stand. In order to fully observe the behavior of the crack front behavior under loading, acrylic specimens are fabricated, with the same sample preparation procedure, and utilized for testing under the four point bending configuration. The specimen used for this investigation is shown below in Figure 36:

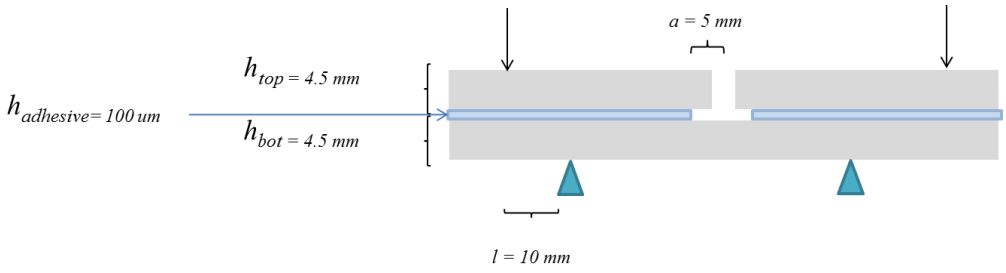

Figure 36. Acrylic multilayer specimen

This multilayer acrylic specimen has both top and bottom substrate thicknesses of 4.5 mm, width of 8 mm, and overall length of 44 mm. The adhesive layer is also the dyed Tra-Bond F114 having a thickness of 100 µm. The pin spacing used for this configuration is 10 mm.

For testing these acrylic specimens, room temperature fatigue loading and main test protocols were followed as mentioned previously in Section 2.4 and Section

2.5. In order to fully visualize the crack front and side of the specimen simultaneously from these acrylic specimens, a 45° mirror prism was placed underneath the specimen in the four point bending test stand. A video camera was focused fully on the prism which displayed the entire pre-defined area and beyond from the bottom substrate due to its transparency.

For fatigue loading, cycles from 5 to 10 N at a displacement rate of 5 mm/min was used until the full pre-defined area was delaminated. A typical cycle count was 200~300 cycles. Detection of this clear delamination was made due pulsing light in the pre-defined area. To follow up with the fatigue loading, main test protocols were conducted in which all five acrylic specimens gave a consistent result in terms of critical loads. Visually the crack will propagate from the center of the width of the specimen where the adhesion strength is evaluated. The average adhesion strength computed from these critical loads in the 3D FEM model came out to be 65.51 J/m^2 with a standard deviation of 9.46 J/m^2. The compiled load-displacement profiles are shown below from the acrylic testing in Figure 37.

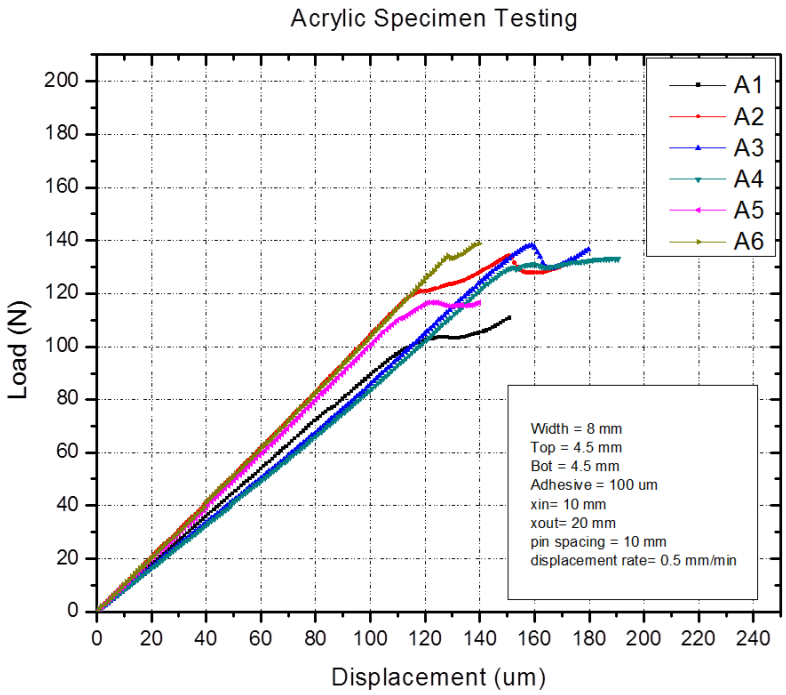

Figure 37. Multilayer acrylic testing

The crack front of a sample acrylic specimen is shown like this in Figure 38 at the end of the test.

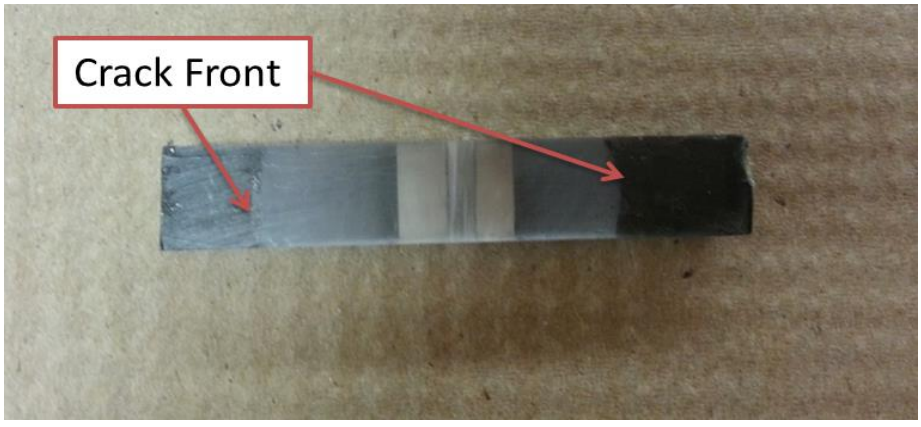

Figure 38. Sample acrylic crack front after testing (bottom view)

To determine the critical load for the adhesion strength evaluation, a criterion is set with regards to the relationship between crack initiation and the load-displacement profile. The compliance change of the load-displacement profile helps determine the critical load as the crack front initially propagates from the pre-defined area. A sample load-displacement profile is shown below in Figure 39 with the slope line as a criterion indicator for obtaining the critical load.

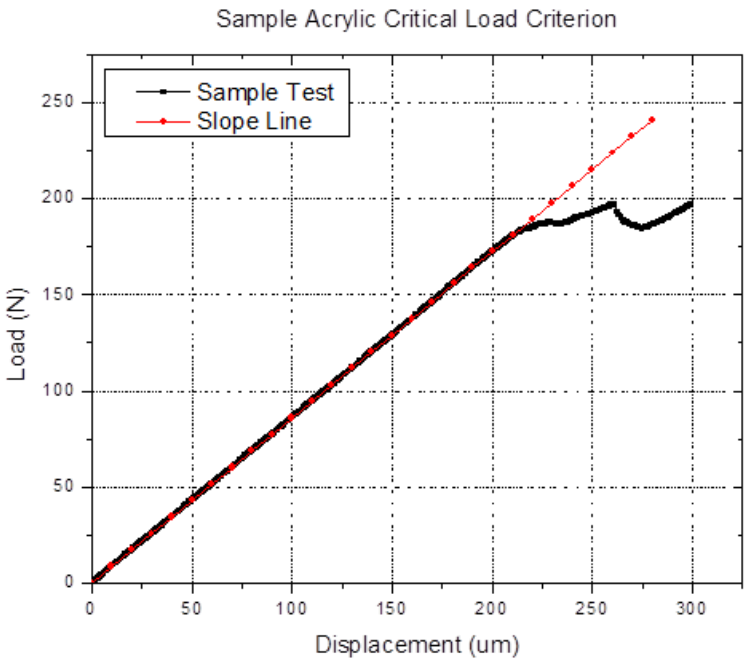

Figure 39. Sample load-displacement profile with slope line

The criterion for obtaining the critical load is the 5% deviation between the slope line and the compliance change from the raw load-displacement curve. Visual recording of the crack initiation supports the correlation between the crack front behavior and the compliance change in the load-displacement profile. The compliance change is

not due to the ductile substrate based off of the evidence from these tests. Since this compliance change has correlation with the crack front initiation with respect to the critical load, this finding is used as a base guideline for other multilayer specimens such as the bronze specimens to obtain the critical load from initial crack propagation.

4.2 *Multilayer rigid/flexible/rigid specimen testing*

Since the acrylic samples have shown the correlation between the crack front behavior and the compliance change, an extension from that experiment can be applied to a rigid-flexible-rigid configuration. For both fatigue loading and main tests, a rigid-flexible-rigid multilayer specimen was used where both adherends and substrates were bronze with the middle adhesive flexible layer as the Tra-Bond F114 epoxy. Test procedures or protocol for both pre-cracking and main test runs were made in collaboration with the Instron Test Stand and its Bluehill software as discussed in Chapter 3. The specimen used for this study is shown below in Figure 40:

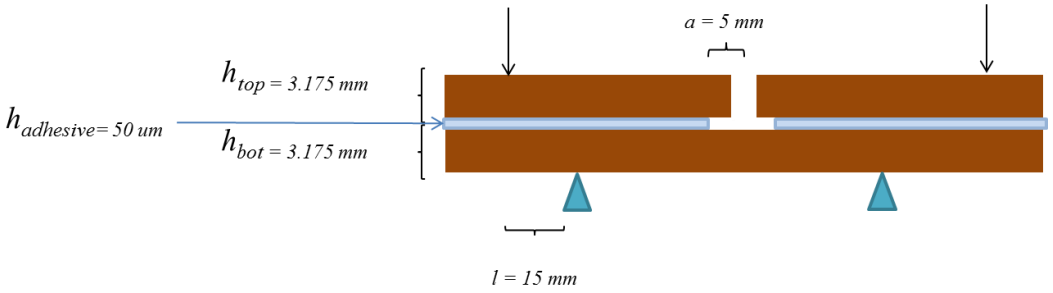

Figure 40. Bronze multilayer specimen

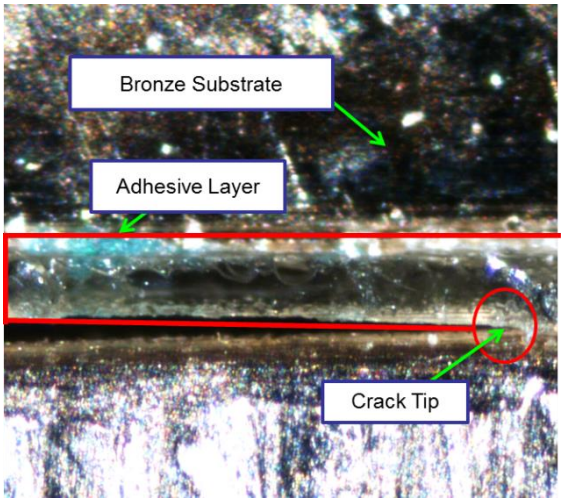

Figure 41. Bronze multilayer specimen right side crack propagation

The multilayer specimen is composed of two bronze adherends or substrates, top and bottom with a thickness of 3.175 mm, width of 12.7 mm, length of 75 mm, with the dyed Tra-Bond F114 adhesive layer having the thickness of 50 µm. The pin spacing used for this configuration is 15 mm. With the fatigue loading cycle test conducted prior to the main test run, the specimen will consist of a pre-crack of 5 mm due to the pre-defined area composed of silicon rubber and deposited aluminum. The visual on crack propagation from the side of the bronze specimen under four point bending is shown above in Figure 41.

4.3 *Room temperature experimental results*

The main experimental batch of 11 bronze samples underwent a room temperature setting during the four point bending test. All 11 samples have gone through the main protocol of creating the pre-crack from the pre-defined area. The main experimental results for a batch of 11 samples are shown in Table 2. The average critical load was found to be 122.24 N with a standard deviation of 8.36 N

yielding a coefficient of variance of 6.8%. The overall batch data is plotted in Figure 42 to show raw load-displacement curves.

Testing Results				
Sample #	Initial Slope (N/um)	Displacement Rate (mm/min)	Critical Moment (N-mm/mm)	Critical Load (N)
1	1.62	0.5	69.99	118.52
2	1.95	0.5	70.98	120.20
3	1.95	0.5	77.35	130.98
4	1.96	0.5	76.00	128.70
5	1.73	0.5	71.68	121.39
6	1.9	0.5	67.67	114.59
7	1.82	0.5	78.68	133.24
9	1.76	0.5	68.96	116.78
10	1.87	0.5	68.44	115.90
11	1.65	0.5	67.98	115.12
12	1.95	0.5	80.03	135.53

Table 2. Room Temperature Experimental Result Table

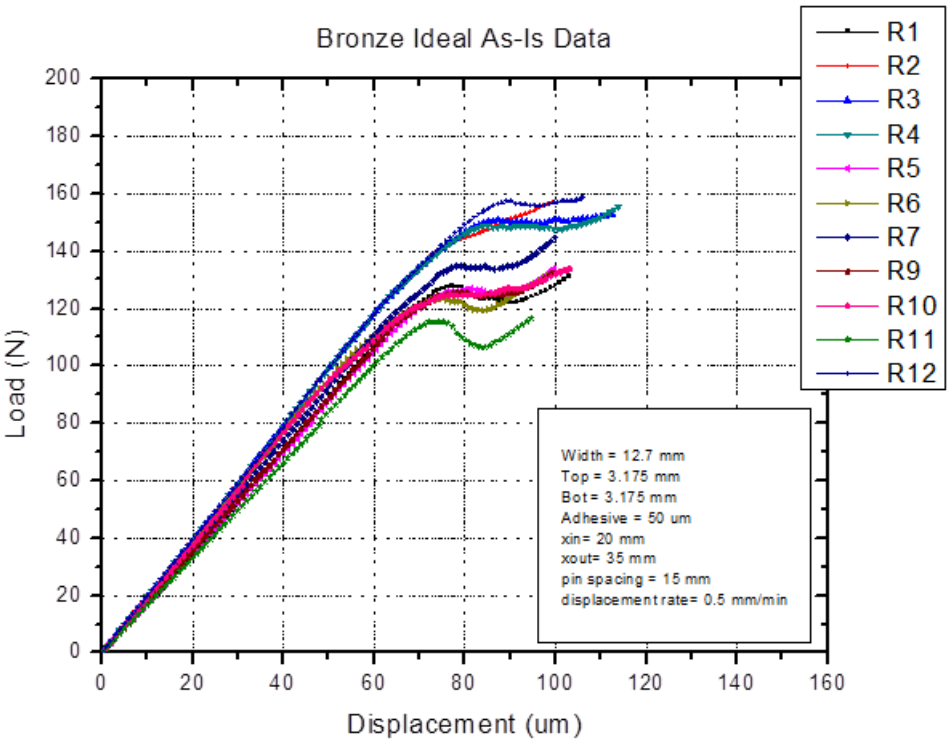

Figure 42. Room temperature bronze sample compilation

From the experimental data and load-displacement plots of each sample tested, the critical load or critical moment is taken into analysis in order to compute the energy release rate. The criterion for gathering each critical load from each sample's data is set in which each critical load is defined as the peak before a load drop where energy is released and crack begins to initiate and propagate.

4.3.1 Room temperature adhesion strength results from modeling

From gathering all the critical loads or moments from each sample test, the energy release rate or J-integral values are computed from ANSYS. The results of the room temperature adhesion strength values are shown below in Table 3.

Sample	1	2	3	4	5	6	7	8	9	10	11
J-Value (J/m²)	3.69	3.80	4.51	4.35	3.87	3.45	4.66	3.58	3.53	3.48	4.83

Table 3. Adhesion Strength Values (Room Temperature)

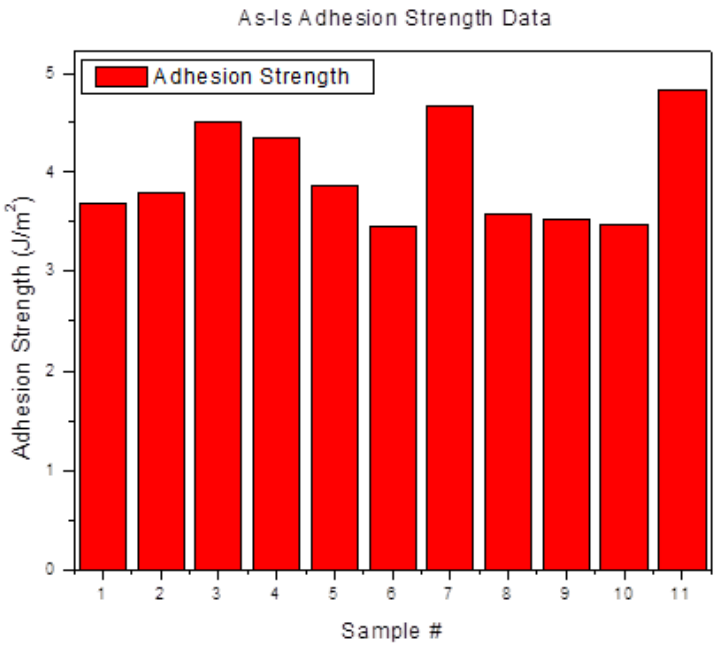

Figure 43. Adhesion Strength Bar Chart (Room Temperature)

As the results show, the average adhesion strength of this batch of 11 found to be 3.98 J/m^2 with a standard deviation of 0.51 J/m^2 yielding a coefficient of variance of 12.8%. With a 12.8% scatter within the adhesion strength values at room temperature, this study has shown drastic improvement in scatter compared to previous literature studies.

4.4 *Extending testing for moisture degradation*

4.4.1 Overview

In addition to the room temperature four point bending test, another batch of 11 samples was subjected to moisture. Before the exposure to moisture, all 11 samples underwent the fatigue pre-crack loading test in order for the pre-crack interface to open for exposure. All 11 samples were then put into a humidity chamber at a condition of 60°C/95%RH for 15 days, where the temperature reaches right above the glass transition temperature of the Tra-Bond F114 in order to loosen the bonds within the adhesive. According to moisture degradation literature review, the adhesion strength of the moisture degraded samples should be lower than that of the adhesion strength of room temperature samples.

4.4.2 Moisture experimental results

After all the 11 samples were exposed to moisture in the humidity chamber for 15 days, the batch was then tested for the main run under four point bending. Critical loads were gathered from each sample test run under the same test protocol as the room temperature test shown below in Table 4. The average critical load was found to be 78.31 N with a standard deviation of 5.45 N yielding a coefficient of variance of 6.9%. Most of the samples in the moisture batch exhibited critical load drops leading to a steady state region plateau. Few others exhibited a sudden change in compliance as the crack initiated with quick propagation. Compliance change of these samples increases with the crack length which was shown in these tests. The overall batch data is plotted in Figure 44 to show raw load-displacement curves.

Testing Results				
Sample #	Initial Slope (N/um)	Displacement Rate (mm/min)	Critical Moment (N-mm/mm)	Critical Load (N)
1	1.35	0.5	41.76	70.72
3	1.52	0.5	45.79	77.53
4	1.32	0.5	41.35	70.02
5	1.50	0.5	46.05	77.98
6	1.40	0.5	50.01	84.69
7	1.27	0.5	49.48	83.79
8	1.28	0.5	48.34	81.87
9	1.53	0.5	42.72	72.35
10	1.37	0.5	43.57	73.77
11	1.22	0.5	47.59	80.60
12	1.45	0.5	50.26	85.11

Table 4. Moisture Experimental Result Table

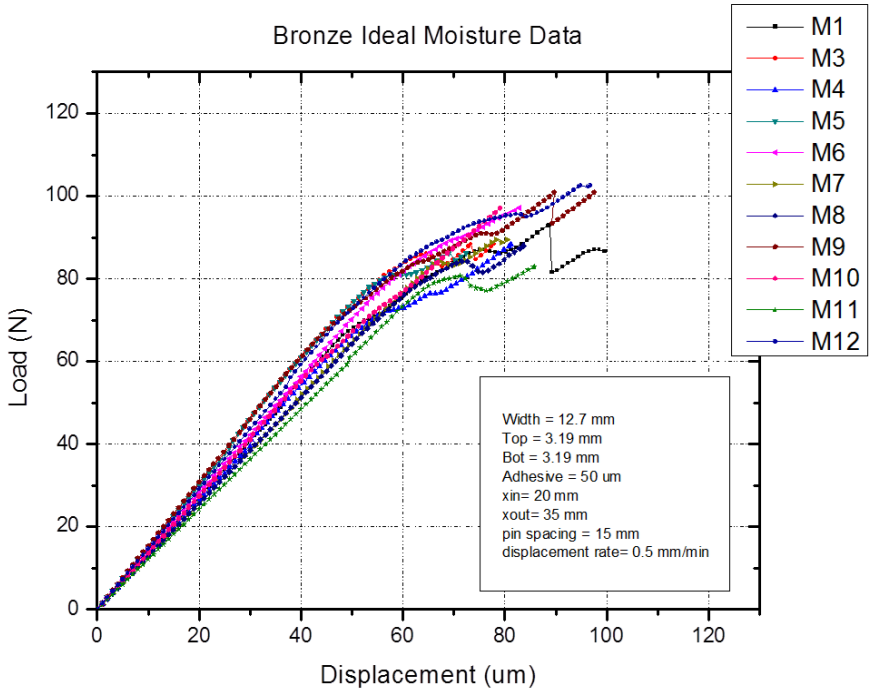

Figure 44. Moisture Degradation Sample Test

Likewise to the room temperature analysis protocol, the critical load or critical moment is taken into analysis in order to compute the energy release rate for the

moisture analysis by ANSYS. The criterion for gathering each critical load is also used with the addition of compliance change where the critical load is taken at the slope change.

4.4.3 Moisture adhesion strength results from modeling

Adhesion strength values are also computed from ANSYS for the moisture batch. The results are shown below in Table 5and Figure 45.

Sample	1	2	3	4	5	6	7	8	9	10	11
J-Value (J/m²)	1.31	1.58	1.29	1.60	1.88	1.84	1.76	1.38	1.43	1.71	1.90

Table 5. Adhesion Strength Values (Moisture Degradation)

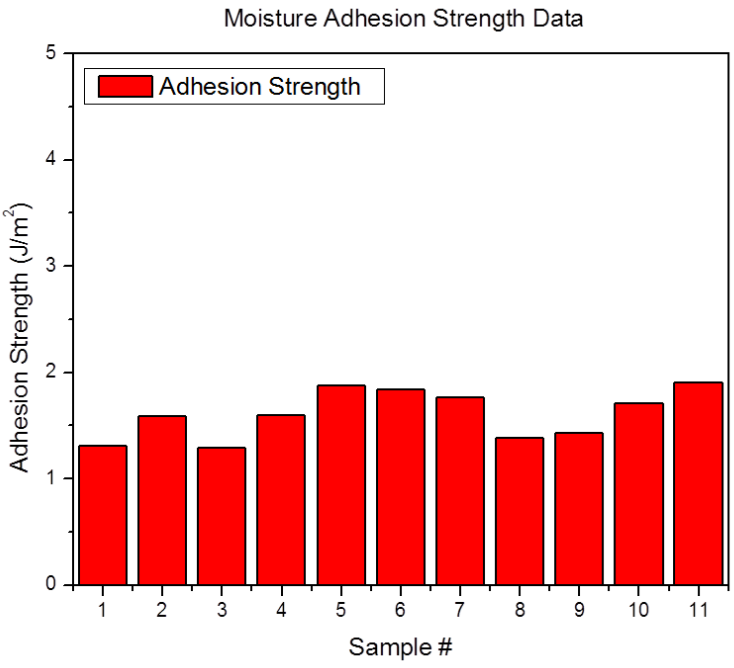

Figure 45. Adhesion Strength Bar Chart (Moisture Degradation)

As the results show above, the average adhesion strength of this moisture batch of 11 found to be 1.61 J/m^2 with a standard deviation of 0.23 J/m^2 yielding a coefficient of variance of 14.3%. These moisture degradation results have proven and verified the drop in adhesion strength when these samples were exposed to moisture.

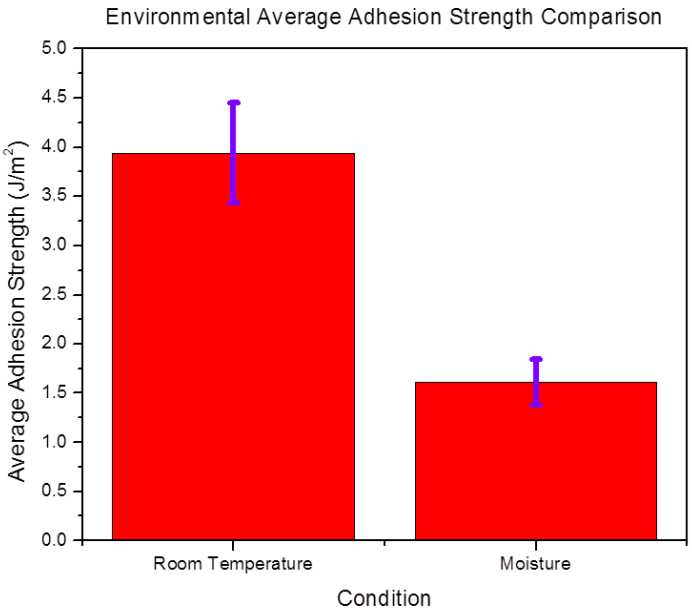

Figure 46. Comparison of adhesion strength values between room temperature and moisture degradation samples

A comparison chart to show this discrepancy of the adhesion strength drop of 60% from room temperature to moisture degradation is shown above in Figure 46.

4.5 *Statistical analysis for adhesion strength data*

4.5.1 Kolmogorov-Smirnov test

Most experimental data from various studies go under an assumption that the data follow an underlying distribution. This invokes a huge risk where if such distribution does not hold that assumption, then the data results attained may be labeled as invalid. Hypotheses and confidence intervals integrated can be off course which affects the data results in its analysis. One of the main approaches that can eliminate this risk is by using a goodness of fit test such as the Kolmogorov-Smirnov test which produces reliable and quantifiable results to help evaluate the underlying distribution of a data set. The Kolmogorov-Smirnov goodness of fit test or K-S test basically decides if a sample or a batch of samples comes from a population with a specific distribution or normal distribution in this case. This K-S goodness of fit test measures and tests for normality of the distribution of a sample data set in which are standardizes and compared with a standard normal distribution [24]. In other words, the K-S test sets the mean and variance of the reference distribution equal to the sample estimates. Like for any other statistical test, there are two hypotheses for the K-S goodness of fit test. The null hypothesis H_0 states that the sample data set follows a normal distribution whereas the alternative hypothesis H_a states that the sample data set does not follow a normal distribution.

In order to verify the null hypothesis, a pre-specified distribution is assumed to be normal for this case. This normal pre-specified cumulative distribution function is said to be $F^*(x)$, in which needs to be compared to an empirical cumulative distribution function $S(x)$.

This empirical function *S(x)* is used as an estimator for the sample data set *F(x),* unknown distribution function shown below [24]:

$$S(x) = \frac{1}{n}\sum_{i=1}^{n} I_{\{x_i \le x\}} \tag{4.5.1}$$

The hypothesized cumulative distribution function *F*(x)* is then compared with *S(x)* to find agreement resulting as a test statistic, *D,* shown below:

$$D = \sup_{x} | F^*(x) - S(x) | \tag{4.5.2}$$

This test statistic, *D,* shows the discrepancy or distance between the empirical function *S(x)* and the hypothesized function *F*(x)* in which is used for the hypotheses testing. The logic of the K-S test states that if the maximum distance between the hypothesized and empirical distribution is small, then the assumed cumulative *F*(x)* will likely be correct. Once the largest vertical distance or discrepancy, *D* test statistic, is found, this is compared to that of a critical region of size $\alpha = 0.05$ which corresponds to values of *D* greater than the 0.95 quartile [24].

Going back to this case study of room temperature and moisture batches, each batch undergoes the K-S test with each getting a *D* statistic. Table 6 and Table 7 below show the computations necessary to get the *D* statistic.

Row	DataSet	Z stat	F_0	F_n	F_{n-1}	D+ =F_n-F_0	D-=F_0-F_{n-1}
1	3.45	-1.02921	0.1539	0.090909	0	-0.062991	0.1539
2	3.48	-0.97065	0.166	0.181818	0.090909091	0.015818	0.0750909
3	3.53	-0.87305	0.1922	0.272727	0.181818182	0.080527	0.0103818
4	3.58	-0.77545	0.2206	0.363636	0.272727273	0.143036	-0.052127
5	3.69	-0.56074	0.2877	0.454545	0.363636364	0.166845	-0.075936
6	3.8	-0.34603	0.3669	0.545455	0.454545455	0.178555	-0.087645
7	3.87	-0.20939	0.4207	0.636364	0.545454545	0.215664	-0.124755
8	4.35	0.727542	0.7642	0.727273	0.636363636	-0.036927	0.1278364
9	4.51	1.039853	0.8485	0.818182	0.727272727	-0.030318	0.1212273
10	4.66	1.332644	0.9082	0.909091	0.818181818	0.000891	0.0900182
11	4.83	1.664474	0.9515	1	0.909090909	0.0485	0.0424091
					Max:	0.215664	0.1539
					D =maximum	0.215664	

Table 6. D statistic computation (Room Temperature Batch)

Row	DataSet	Z stat	F_0	F_n	F_{n-1}	D+ =F_n-F_0	D-=F_0-F_{n-1}
1	1.29	-1.38997	0.082416	0.090909	0	0.008493	0.082416
2	1.31	-1.30235	0.096458	0.181818	0.090909091	0.08536	0.0055489
3	1.38	-0.99568	0.159868	0.272727	0.181818182	0.112859	-0.02195
4	1.43	-0.77663	0.218874	0.363636	0.272727273	0.144762	-0.053853
5	1.58	-0.11948	0.452638	0.454545	0.363636364	0.001907	0.0890016
6	1.6	-0.03186	0.487635	0.545455	0.454545455	0.05782	0.0330895
7	1.71	0.450049	0.6736	0.636364	0.545454545	-0.037236	0.1281455
8	1.76	0.669099	0.7454	0.727273	0.636363636	-0.018127	0.1090364
9	1.84	1.019579	0.8438	0.818182	0.727272727	-0.025618	0.1165273
10	1.88	1.194819	0.883	0.909091	0.818181818	0.026091	0.0648182
11	1.9	1.282439	0.8997	1	0.909090909	0.1003	-0.009391
					Max:	0.144762	0.1281455
					D =maximum	0.144762	

Table 7. D statistic computation (Moisture Degradation Batch)

For the room temperature batch, the D statistic comes out to be 0.216 which gets compared to the critical region of α=0.05. From a K-S critical region table at *N*=11, the critical value is 0.41. As for the moisture degradation batch, the *D* statistic turns out to be 0.145 also gets compared to the critical region of α=0.05. Since the room temperature and moisture degradation's D statistic of 0.216 and 0.145, respectively, are less than the critical region value of 0.41, the null hypothesis does

not get rejected. Therefore, both the room temperature and the moisture degradation sample set follow a normal distribution as shown below in both Figure 47 and Figure 48.

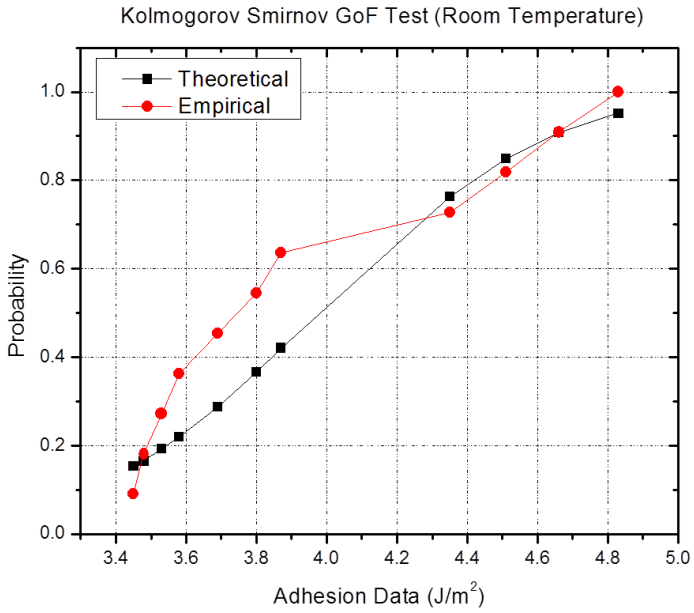

Figure 47. K-S Goodness of Fit Test (Room Temperature)

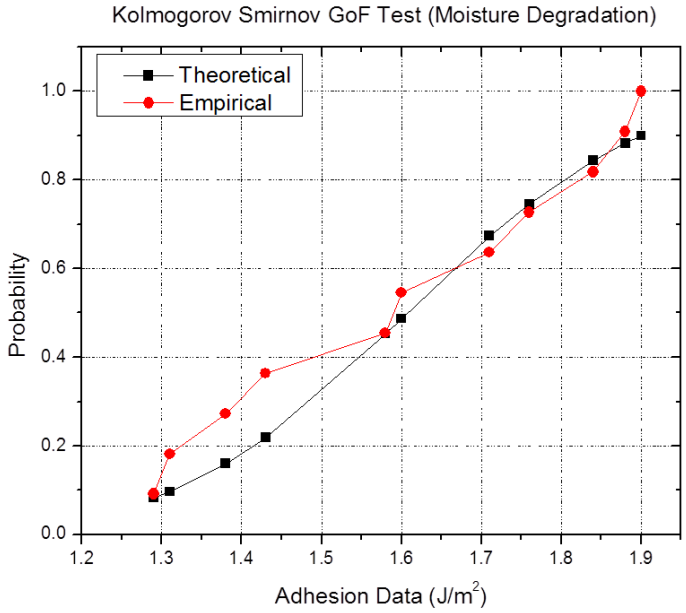

Figure 48. K-S Goodness of Fit Test (Moisture Degradation)

4.5.2 One-way Analysis of Variance (ANOVA) test

In relation to the K-S goodness of fit test to verify normality of both sample batches, one-way analysis of variance (ANOVA) test can be conducted to test both means assuming the populations are normally distributed. The purpose of this ANOVA test is to compare the means of two or more samples of data to infer if the means are statistically the same or different. Specifically, ANOVA tests the null hypothesis:

$$H_0 : \mu_1 = \mu_2 = \mu_3 = ... = \mu_\kappa \tag{4.5.3}$$

where μ is the data set mean or group mean and κ is the number of data sets or groups. If however by any means the ANOVA gives out a significant result, the alternative hypothesis becomes accepted where at least two group means are significantly different from each other [25]. The main statistic that is used for the hypothesis test in ANOVA is the *F*-statistic. The null hypothesis, H_0, becomes rejected if the main *F*-statistic from the data is greater than the critical *F*-statistic, F_α or if the main F-statistic's p value is less than the critical region $\alpha = 0.05$.

The F-statistic is defined as:

$$F = \frac{s_b^{\,2}}{s_w^{\,2}} \tag{4.5.4}$$

where F is the ratio of two sample variances divided by their respective degrees of freedom. In other words, the F statistic is found by dividing the between group variance by the within group variance. The between group variation *SS(B)*, also known as Sum of Squares Between groups, is the variation due to the interaction between the samples shown here:

$$SS(B) = \sum n\left(\bar{x} - \bar{X}_{GM}\right)^2 \tag{4.5.5}$$

where $\bar{X}_{GM}$ is the grand mean of a set of samples. The variance due to the interaction between the samples is marked as *MS(B)* for Mean Square Between groups, s_b^2. If the sample means are proximate to each other, then the *SS(B)* will be small. There are *k* samples involved with one data value for each sample in which brings out the *k-1* degrees of freedom [25].

The other half of the F-statistic computation is the variation due to the differences within individual samples marked as *MS(W)* for Mean Square Within groups, s_w^2. In order to get *MS(W)*, the Sum of Squares Within groups, *SS(W)* must be computed. This undergoes an assumption that each sample is considered independent with no interaction between samples. The Sum of Squares Within groups is shown here:

$$SS(W) = \sum df * s^2 \tag{4.5.6}$$

where the degrees of freedom is equal to the sum of the individual degrees of freedom for each sample which makes *df* equal to *k* less than the total sample size. With all these ANOVA parameters introduced, a summary table is needed to keep track of the values needed to compute the F-statistic shown below in Table 8:

	SS	*df*	*MS*	*F*
Between	$SS(B)$	$k-1$	$\frac{SS(B)}{k-1}$	$\frac{MS(\mathrm{B})}{MS(W)}$
Within	$SS(W)$	$N-k$	$\frac{SS(W)}{N-k}$	
Total	$SS(W)+SS(B)$	$N-1$		

Table 8. ANOVA Parameters

From the two sample batches, one from room temperature and the other from moisture degradation, the adhesion strength data were conducted through ANOVA which was summarized with this table shown below:

Anova: Single Factor						
SUMMARY						
Groups	*Count*	*Sum*	*Average*	*Variance*		
Column 1	11	43.75	3.977273	0.262462		
Column 2	11	17.68	1.607273	0.052102		
ANOVA						
ce of Varia	*SS*	*df*	*MS*	*F*	*P-value*	*F crit*
Between G	30.89295	1	30.89295	196.4178	8.36E-12	4.351244
Within Gro	3.145636	20	0.157282			
Total	34.03859	21				

Table 9. ANOVA Summary Table (Adhesion Strength Data)

As a result, the *p*-value came out to be $8.36\text{x}10^{-12}$ which is much less than the critical region *p*-value of 0.05 which rejects the null hypothesis. Therefore, it is safe to say that the adhesion strength mean of room temperature samples is significantly different than the adhesion strength mean of moisture degradation samples.

CHAPTER 5: CONCLUSIONS

The four point bending test was commonly used as an approach to evaluate the adhesion strength by taking advantage of the constant stress fields along the crack length. An extension of these previous works that have conducted on bilayer systems was proposed and implemented onto multilayer structures with a predefined area in order to characterize the adhesion strength between the polymer adhesive and rigid substrates. The predefined area allows for a weak adhesion horizontal accurate pre-crack which allows crack propagation under four point bending as well as reducing scatter within the values of critical loads. This predefined area in addition allows for stable crack propagation at a load plateau without going through an initial load overshoot compared to previous studies' configurations. A numerical analysis was conducted to compute the energy release rate from the critical loads using the concept of the J-integral under non plane strain conditions.

Under this non plane strain condition, a set of acrylic specimens were fabricated for the purpose of investigating the crack front behavior under four point bending. This crack front behavior was in conjunction with the compliance change of the load-displacement profile as the initial crack begins to propagate. This compliance change was concluded to be in correlation with the crack propagation at the center of the specimen. The numerical model was able to pinpoint the adhesion strength values through half the width of the specimen where only the adhesion strength value at the center of the width was the primary focus.

In addition, metal substrates were tested under environmental conditions by using the acrylic configuration analysis as a base guideline. Experimental results

along with visual evidence support the consistent behavior between crack front behavior and compliance change for both acrylic and bronze specimens. This correlation can be used as a baseline for testing other electronic packages for interfacial failure.

APPENDICES

Appendix A: ANSYS 3D Quarter Model of 4PB Sample –Same Top and Bottom Heights (Used for both Acrylic and Bronze)

```
!*****************************************************************************
!Top Acrylic Layer (4.5 mm)
!F114 Adhesive (100 um)
!Bottom Acrylic Layer (4.5 mm)
!Interfacial crack between Bottom Acrylic and F114 layers

! Mesh sensitivity review orignilly formed to determine minimum
!    elements for a mesh insensitive model
!  /input,'D:\LOMSS
Workstation\Documents\Stephen\Code\4PB_3D_Ac_sameTB',txt
!################################################
!fini
!/clear
output_file='4PB_Ac_sameTB'     !Output File Name
elm_thick=5
z_ratio=25
!Load = 125
!################################################
! Define Parameters (Units: N-mm-sec-K)
!################################################
width=8
Moment=50     !N-mm

/filname,output_file,db
! Geometric Parameters
a_crack=5     !mm
x_in=10     !mm
x_out=20     !mm
Pin_Space=x_out - x_in     !mm
length=22     !mm

h_PSR=0.100     !mm
h_Support_Top=4.5     !mm
h_Support_Bot=4.5     !mm
```

```
ratio=1     !mm
h_EMC=1     !mm
x_fine=0.4    !mm
y_fine=x_fine/ratio     !mm

h_in=h_PSR*2     !mm
w_in=h_in*ratio     !mm
r_mill=1     !
! Position Parameters
y1=0     !mm
y2=y1 + h_Support_Bot     !mm
y3=y2 + h_EMC-y_fine     !mm
y4=y2 + h_EMC-h_in     !mm
y5=y2+ h_EMC     !mm
y6=y5 + h_PSR     !mm
y7=y6 + h_in     !mm
y8=y6 + y_fine     !mm
y9=y8 + h_Support_Top     !mm

x1=0     !mm
x22=r_mill     !mm
x2=a_crack - x_fine     !mm
x3=a_crack - w_in     !mm
x4=a_crack     !mm
x5=a_crack + w_in     !mm
x6=a_crack + x_fine     !mm
x7=x_in     !mm
x8=x_out     !mm
x9=length     !mm

z0=0     !mm

y_bot=y1     !mm
y_crack=y5     !mm
y_top=y9     !mm
x_start=x1     !mm
x_crack=x4     !mm
x_in=x7     !mm
x_end=x9     !mm

z_mid=0     !mm
z_end=-width/2     !mm


!################################################
! Coordinate Systems
```

```
local,22,0,x_crack,y_crack        ! Define cylindrical coordinates around Right crack
tip
local,23,1,x_crack,y_crack        ! Define cylindrical coordinates around Right crack
tip
csys,0
!################################################
! Mesh Control Parameters
!################################################
aspect_in=20  !10
esize_max=h_PSR/elm_thick*z_ratio
tol=0.000001     !mm
max_in_size = h_PSR/elm_thick*aspect_in
    !
KSCON_rad=h_PSR/elm_thick/2     !mm
elm_a=w_in/(h_PSR/elm_thick)     !
elm_b=h_in/(h_PSR/elm_thick)     !
elm_c=elm_thick     !

elm_PSR=elm_thick     !
elm_EMC_Bot=(h_EMC-y_fine)/(max_in_size)     !
elm_Support_Top=h_Support_Top/max_in_size    !
elm_Support_Bot=h_Support_Bot/max_in_size     !
elm_y_fine = (y_fine)/(max_in_size)

esize_long=max_in_size  !esize_max
elm_122=NINT((x22-x1)/esize_long)      !
elm_222=NINT((x2-x22)/esize_long)      !
elm_67=NINT((x7-x6)/esize_long)      !
elm_78=NINT((x8-x7)/esize_long)      !
elm_89=NINT((x9-x8)/esize_long)      !

esize_z=esize_max
width_esize=(width/2)/esize_z     !

!################################################
! Preprocessing Section
!################################################
/prep7
!################################################
!  Created Element Types
!################################################
ET,1,186
ET,2,200,7           ! MESH 200 ELEMENT
ET,3,156,           ! Surface 156 Strucutral Surface Line Load Effect
KEYOPT,3,2,0
  KEYOPT,3,4,0
```

```
 KEYOPT,3,7,1    ! for large deflection analysis use original area
!###############################################
!  Material Properties
!###############################################
!Material 2
E_2=2500     !
nu_2=0.38     !
mat_PSR=2     !Material ID
EX,mat_PSR,E_2     !Modulus (MPa)
nuxy,mat_PSR,nu_2     !Poisson's Ratio
!###############################################
!Material 1
E_Acrylic=3500
nu_Acrylic=0.35
mat_PCB=1     !Material ID
EX,mat_PCB,E_Acrylic  !26341     !Modulus (MPa)
nuxy,mat_PCB,nu_Acrylic !0.33 !0.22     !Poisson's Ratio
!###############################################
!Material 3
mat_EMC=3     !Material ID
EX,mat_EMC,E_Acrylic  !22000     !Modulus (MPa)
nuxy,mat_EMC,nu_Acrylic !0.28     !Poisson's Ratio
!###############################################
!Material 4
mat_Support_top=4     !Material ID
EX,mat_Support_top,E_Acrylic  !70000     !Modulus (MPa)
nuxy,mat_Support_top,nu_Acrylic !0.33     !Poisson's Ratio
!###############################################
!Material 4
mat_Support_bot=5     !Material ID
EX,mat_Support_bot,E_Acrylic  !70000     !Modulus (MPa)
nuxy,mat_Support_bot,nu_Acrylic !0.33     !Poisson's Ratio
!###############################################

!###############################################
! Keypoints
!###############################################
k,11,x1,y1,z0
k,12,x1,y2,z0
k,13,x1,y3,z0
k,14,x1,y4,z0
k,15,x1,y5,z0
k,16,x1,y6,z0
k,17,x1,y7,z0
k,18,x1,y8,z0
k,19,x1,y9,z0
```

k,21,x2,y1,z0
k,22,x2,y2,z0
k,23,x2,y3,z0
k,24,x2,y4,z0
k,25,x2,y5,z0
k,26,x2,y6,z0
k,27,x2,y7,z0
k,28,x2,y8,z0
k,29,x2,y9,z0
k,34,x3,y4,z0
k,35,x3,y5,z0
k,36,x3,y6,z0
k,37,x3,y7,z0
k,41,x4,y1,z0
k,42,x4,y2,z0
k,43,x4,y3,z0
k,44,x4,y4,z0
k,45,x4,y5,z0
k,46,x4,y6,z0
k,47,x4,y7,z0
k,48,x4,y8,z0
k,49,x4,y9,z0
k,54,x5,y4,z0
k,55,x5,y5,z0
k,56,x5,y6,z0
k,57,x5,y7,z0
k,61,x6,y1,z0
k,62,x6,y2,z0
k,63,x6,y3,z0
k,64,x6,y4,z0
k,65,x6,y5,z0
k,66,x6,y6,z0
k,67,x6,y7,z0
k,68,x6,y8,z0
k,69,x6,y9,z0
k,71,x7,y1,z0
k,72,x7,y2,z0
k,73,x7,y3,z0
k,74,x7,y4,z0
k,75,x7,y5,z0
k,76,x7,y6,z0
k,77,x7,y7,z0
k,78,x7,y8,z0
k,79,x7,y9,z0
k,81,x8,y1,z0
k,82,x8,y2,z0

```
k,83,x8,y3,z0
k,84,x8,y4,z0
k,85,x8,y5,z0
k,86,x8,y6,z0
k,87,x8,y7,z0
k,88,x8,y8,z0
k,89,x8,y9,z0
k,91,x9,y1,z0
k,92,x9,y2,z0
k,93,x9,y3,z0
k,94,x9,y4,z0
k,95,x9,y5,z0
k,96,x9,y6,z0
k,97,x9,y7,z0
k,98,x9,y8,z0
k,99,x9,y9,z0
k,221,x22,y1,z0
k,222,x22,y2,z0
k,223,x22,y3,z0
k,224,x22,y4,z0
k,225,x22,y5,z0
k,226,x22,y6,z0
k,227,x22,y7,z0
k,228,x22,y8,z0
k,229,x22,y9,z0

!For different keypoints at the crack tip
!These keypoints are used by the Top layer
k,9915,x1,y5,z0
k,9925,x2,y5,z0
k,9935,x3,y5,z0
k,99225,x22,y5,z0

!################################################
! Lines
!################################################
/PNUM,KP,1
/PNUM,LINE,1
/PNUM,AREA,1
LPLOT

!y1 - Horizontal Lines Bottom of Bottom Support Layer
l,221,11,elm_122        !1
l,21,221,elm_222        !2
l,41,21,elm_a       !3
l,41,61,elm_a       !4
```

```
l,61,71,elm_67        !5
l,71,81,elm_78        !6
l,81,91,elm_89        !7

!y2 - Horizontal Lines Bottom of EMC Layer
l,222,12,elm_122      !8
l,22,222,elm_222      !9
l,42,22,elm_a        !10
l,42,62,elm_a        !11
l,62,72,elm_67       !12
l,72,82,elm_78       !13
l,82,92,elm_89       !14

!y3 -Horizontal Lines Middle of EMC
l,223,13,elm_122      !15
l,23,223,elm_222      !16
l,43,23,elm_a        !17
l,43,63,elm_a        !18
l,63,73,elm_67       !19
l,73,83,elm_78       !20
l,83,93,elm_89       !21

!y4 - Horizontal Lines (inside concentration in EMC)
l,44,34,elm_a        !22
l,44,54,elm_a        !23

!y5 - Horizontal Lines (Top of EMC  Layer)
l,225,15,elm_122      !24
l,25,225,elm_222      !25
l,35,25,elm_c        !26
l,45,35,elm_a        !27
l,45,55,elm_a        !28
l,55,65,elm_c        !29
l,65,75,elm_67       !30
l,75,85,elm_78       !31
l,85,95,elm_89       !32

!y6 - Horizontal Lines Top of PSR Layer
l,26,226,elm_222      !33
l,36,26,elm_c        !34
l,46,36,elm_a        !35
l,46,56,elm_a        !36
l,56,66,elm_c        !37
l,66,76,elm_67       !38
l,76,86,elm_78       !39
l,86,96,elm_89       !40
```

```
!y5 - Horizontal Lines Top of PSR Layer For Top CRACK
l,9925,99225,elm_222          !41
l,9935,9925,elm_c          !42
l,45,9935,elm_a          !43


l,47,37,elm_a          !44
l,47,57,elm_a          !45

!y8 - Horizontal Lines Top of PCB
l,28,228,elm_222          !46
l,48,28,elm_a          !47
l,48,68,elm_a          !48
l,68,78,elm_67          !49
l,78,88,elm_78          !50
l,88,98,elm_89          !51

!y9 - Horizontal Lines Top of Top Support
l,29,229,elm_222          !52
l,49,29,elm_a          !53
l,49,69,elm_a          !54
l,69,79,elm_67          !55
l,79,89,elm_78          !56
l,89,99,elm_89          !57


!Vertical Lines x1
l,12,11,elm_Support_Bot          !58
l,13,12,elm_EMC_bot          !59
l,15,13,elm_b          !60


l,222,221,elm_Support_Bot          !61
l,223,222,elm_EMC_bot          !62
l,225,223,elm_b          !63
l,226,99225,elm_PSR          !64
l,228,226,elm_b          !65
l,229,228,elm_Support_Top          !66


l,22,21,elm_Support_Bot          !67
l,23,22,elm_EMC_bot          !68
l,25,23,elm_b          !69
l,26,9925,elm_PSR          !70
l,28,26,elm_b          !71
```

```
l,29,28,elm_Support_Top         !72

!Vertical Lines x3
l,35,34,elm_b         !73
l,36,9935,elm_PSR         !74
l,36,37,elm_b         !75

!Vertical Lines x4
l,42,41,elm_Support_Bot         !76
l,43,42,elm_EMC_bot         !77
l,44,43,elm_c         !78
l,45,44,elm_b         !79
l,46,45,elm_PSR         !80
l,47,46,elm_b         !81
l,48,47,elm_c         !82
l,49,48,elm_Support_Top         !83

!Vertical Lines x5
l,55,54,elm_b         !84
l,56,55,elm_PSR         !85
l,56,57,elm_b         !86

!Vertical Lines x6
l,62,61,elm_Support_Bot         !87
l,63,62,elm_EMC_bot         !88
l,65,63,elm_b         !89
l,66,65,elm_PSR         !90
l,68,66,elm_b         !91
l,69,68,elm_Support_Top         !92

!Vertical Lines x7
l,72,71,elm_Support_Bot         !93
l,73,72,elm_EMC_bot         !94
l,75,73,elm_b         !95
l,76,75,elm_PSR         !96
l,78,76,elm_b         !97
l,79,78,elm_Support_Top         !98

!Vertical Lines x8
l,82,81,elm_Support_Bot         !99
l,83,82,elm_EMC_bot         !100
l,85,83,elm_b         !101
l,86,85,elm_PSR         !102
l,88,86,elm_b         !103
l,89,88,elm_Support_Top         !104
```

```
!Vertical Lines x9
l,92,91,elm_Support_Bot         !105
l,93,92,elm_EMC_bot         !106
l,95,93,elm_b         !107
l,96,95,elm_PSR         !108
l,98,96,elm_b         !109
l,99,98,elm_Support_Top         !110

!Slanted Lines EMC
l,34,23,         !111
l,54,63,         !112

!Slanted Lines PCB
l,37,28,         !113
l,57,68,         !114



!################################################
! Areas from Lines
!################################################

! Areas for Bottom Support Layer
al,1,58,8,61,         !1
al,2,61,9,67,         !2
al,3,67,10,76,         !3
al,4,76,11,87,         !4
al,5,87,12,93,         !5
al,6,93,13,99,         !6
al,7,99,14,105,         !7

! Areas for Bottom Part of EMC Layer
al,8,59,15,62,         !8
al,9,62,16,68,         !9
al,10,68,17,77,         !10
al,11,77,18,88,         !11
al,12,88,19,94,         !12
al,13,94,20,100,         !13
al,14,100,21,106,         !14

! Areas for Top EMC for Concentration
al,15,60,24,63,         !15
al,16,63,25,69,         !16
al,111,69,26,73,         !17
al,17,111,22,78,         !18
al,18,78,23,112,         !19
```

```
al,84,112,29,89,         !20
al,22,73,27,79,         !21
al,23,79,28,84,         !22
al,19,89,30,95,         !23
al,20,95,31,101,         !24
al,21,101,32,107,         !25

! Areas for PSR Layer
al,41,64,33,70,         !26
al,42,70,34,74,         !27
al,43,74,35,80,         !28
al,28,80,36,85,         !29
al,29,85,37,90,         !30
al,30,90,38,96,         !31
al,31,96,39,102,         !32
al,32,102,40,108,         !33

! Areas for PCB Layer
al,33,65,46,71,         !34
al,34,71,113,75,         !35
al,44,113,47,82,         !36
al,45,82,48,114,         !37
al,37,86,114,91,         !38
al,35,75,44,81,         !39
al,36,81,45,86,         !40
al,38,91,49,97,         !41
al,39,97,50,103,         !42
al,40,103,51,109,         !43

! Areas for Top Support Layer
al,46,66,52,72,         !44
al,47,72,53,83,         !45
al,48,83,54,92,         !46
al,49,92,55,98,         !47
al,50,98,56,104,         !48
al,51,104,57,110,         !49
!################################################
! Define Materals from Areas
!################################################
! EMC
asel,,loc,y,y2,y5
aATT,mat_EMC

! PSR
asel,,loc,y,y5,y6
aATT,mat_PSR
```

```
! PCB
asel,,loc,y,y6,y8
aATT,mat_PCB

! Support
asel,,loc,y,y1,y2
aATT,mat_Support_top

! Support
asel,,loc,y,y8,y9
aATT,mat_Support_bot

alls
!################################################
!    Meshing
!################################################
type,2
alls
MSHKEY,1
MSHAPE,0,2D
amesh,all
!################################################
TYPE,1
ESIZE,,width_esize
EXTOPT,ON
VEXT,all,,,,, -width/2,,,
alls
!################################################
! Create Surface Elements for Line Loading at x_out
!################################################
type,3
lsel,,loc,y,y_top-tol,y_top+tol
lsel,r,loc,x,x_out-tol,x_out+tol
*get,line_out,LINE,,num,min

ksel,,loc,y,y_bot-tol,y_bot+tol
ksel,r,loc,x,x_out-tol,x_out+tol
ksel,r,loc,z,z_mid+tol,z_mid-tol
*get,KB,KP,,num,min

ksel,,loc,y,y_bot-tol,y_bot+tol
ksel,r,loc,x,x_out-tol,x_out+tol
ksel,r,loc,z,z_end+tol,z_end-tol
*get,KE,KP,,num,min
```

```
LATT,mat_Support_top,1,3,,KB,KE
LESIZE,line_out,,,width_esize,,0
lmesh,line_out

esel,,type,,3
cm,Line_Out_elem,ELEM
nsle
nsel,r,loc,z,z0-tol,z0+tol
*get,nod_out,node,,num,min
!################################################
! Select Nodes to Create Components
!################################################
! Component for node of outer pin (line load over Z direction)
nsel,,loc,y,y_bot-tol,y_crack+tol
nsel,r,loc,x,x_start-tol,x_start+tol
cm,FIX_X,NODE

nsel,,loc,y,y_bot-tol,y_bot+tol
nsel,r,loc,x,x_in-tol,x_in+tol
cm,FIX_Y,NODE

nsel,,loc,z,z_mid-tol,z_mid+tol
cm,Fix_Z,NODE


nsel,,loc,y,y_crack-tol,y_crack+tol
nsel,r,loc,x,x_crack-tol,x_crack+tol
CM,crackfront,NODE

/sol
CINT,NEW,1 ! DEFINE CRACK ID
CINT,TYPE,VCCT
CINT,CTNC,crackfront ! DEFINE CRACK TIP NODE COMPONENT
CINT,SYMM,OFF ! SYMMETRY OFF
CINT,NORMAL ! DEFINE CRACK PLANE NORMAL
CINT,LIST


alls                        ! Select all nodes
*get,num_nods,node,,COUNT
*get,num_elm,ELEM,,COUNT



    /sol            ! Enter solution section
```

```
    ANTYPE,0          ! Specify static analysis
    nlgeom,off        ! Turn off non linear geometries
    autots,on         ! Turn ON auto time step
    kbc,0             ! Specify stepped or ramped loading within a load step (0=Ramp)
    outres,all,all    ! Output all data in last time step
    time,1            ! Specify time span of analysis
    d,FIX_X,UX        ! Set UX displacement equal to zero
    d,FIX_Y,UY        ! Set UY displacement equal to zero
    d,FIX_Z,UZ        ! Set UZ displacement equal to zero


  elm_load=(Load/2/width)
  SFE,Line_Out_elem,3,PRES,,elm_load

  !DL,line_out,209,UY,-0.200
    solv


/post1
prcint,1

/post1
    pts_rad=h_psr*18/10
    ab_ratio=10
    /input,'D:\LOMSS Workstation\Documents\Stephen\4PB\jint',txt

*get,y_out,node,nod_out,u,y
!################################################
SAVE,output_file,db
!################################################
```

Appendix B: ANSYS Virtual Crack Closure Technique (VCCT) Code for 3D Model

```
!*************************************************************************
*
!                    J_VCCT_3D File
!      Solves J and VCCT along 3D Crack Front at each node
!  /input,'D:\LOMSS Workstation\Documents\Stephen\Code\J_VCCT_3D',txt
!*************************************************************************
*

/post1
alls

!Create component of Z axis crack tip nodes
nsel,,loc,x,x_crack-tol,x_crack+tol
nsel,r,loc,y,y_crack-tol,y_crack+tol
*get,J_nods,node,,COUNT
cm,Jz_nodes,NODE

csys,0
*DIM,DIS_LAB,CHAR,1,7
*DIM,DIS_INFO,,J_nods,7

DIS_LAB(1,1)= 'z_pos'
DIS_LAB(1,2)= 'z/W'
DIS_LAB(1,3)= 'Jint'
DIS_LAB(1,4)= 'G_I'
DIS_LAB(1,5)= 'G_II'
DIS_LAB(1,6)= 'G_III'
DIS_LAB(1,7)= 'G_Total'


*DO,ii,1,J_nods
  ! Select next node along Z axis
  CMSEL,,Jz_nodes
  *get,crack_z,node,,MXLOC,Z
  nsel,,loc,x,x_crack-tol,x_crack+tol
  nsel,r,loc,y,y_crack-tol,y_crack+tol
  nsel,r,loc,z,crack_z-tol,crack_z+tol
  *get,current_nod,node,,num,min
  alls

!Find VCCT Parameters at current_nod
```

```
*GET,G1,CINT,1,,current_nod,,,,G1
G_I=1000*G1
*GET,G2,CINT,1,,current_nod,,,,G2
G_II=1000*G2
*GET,G3,CINT,1,,current_nod,,,,G3
G_III=1000*G3
*GET,GT,CINT,1,,current_nod,,,,GT
G_total=1000*GT

  !Find J at current_nod
/input,'D:\LOMSS Workstation\Documents\Stephen\Code\jint_3D',txt

! Assign Values to Data Table
  *VFILL,DIS_INFO(ii,1),DATA,crack_z
  *VFILL,DIS_INFO(ii,2),DATA,(ii-1)/(J_nods-1)
  *VFILL,DIS_INFO(ii,3),DATA,Jint_3D
  *VFILL,DIS_INFO(ii,4),DATA,G_I
  *VFILL,DIS_INFO(ii,5),DATA,G_II
  *VFILL,DIS_INFO(ii,6),DATA,G_III
  *VFILL,DIS_INFO(ii,7),DATA,G_total

  !Redefind remaining z axis nodes
  nsel,,loc,x,x_crack-tol,x_crack+tol
  nsel,r,loc,y,y_crack-tol,y_crack+tol
  nsel,r,loc,z,crack_z-tol,Z_end-tol
  CM,Jz_nodes,NODE

*ENDDO

save_file='Pull_3D_noAL_Mesh'
!*****************************************************************
!SAVE,filename,db
!*****************************************************************
*****
! Write Results to File
!*****************************************************************
*****
fini
parsav,all,par.txt
/clear
parres,,par.txt

*cfopen,output_file,csv,,APPEND

*VWRITE,'Case','width','elm_PSR','z_ratio','num_elms','Load'
%C,%C,%C,%C,%C,%C
```

```
*VWRITE,'4PB',width,elm_PSR,z_ratio,num_elm,Load
%C,%G,%G,%G,%G,%G

*VWRITE,DIS_LAB(1,1),DIS_LAB(1,2),DIS_LAB(1,3),DIS_LAB(1,4),DIS_LAB(
1,5),DIS_LAB(1,6),DIS_LAB(1,7)
%C,%C,%C,%C,%C,%C,%C

*VWRITE,DIS_INFO(1,1),DIS_INFO(1,2),DIS_INFO(1,3),DIS_INFO(1,4),DIS_IN
FO(1,5),DIS_INFO(1,6),DIS_INFO(1,7)
%G,%G,%G,%G,%G,%G,%G

*cfclos,output_file,csv
!*************************************************************************
*****
```

Appendix C: ANSYS J-Integral Computation Code

```
!************************Calculate J
Integral*****************************
!   /input,'D:\LOMSS Workstation\Documents\Stephen\Code\jint_3D',txt
! This file is called jint.txt
! This program will solve for the J-integral around the crack tip
! Must specify the adhesive layer thickness
! Will use an b/a ratio of 0.1 to solve
! a must be at least 3 element lengths from the cr ack tip
!  Output is in J/m^2
!*****************************************************************
*****

!################################################
! Inputs for Solve
!################################################
crack_x=x_crack
crack_y=y_crack
!crack_z=z0
!################################################
csys,0
/UIS,MSGPOP,3
!################################################
/post1                  ! Enter Post Processing Section
  alls                  ! Select all nodes
  etable,sene,sene            ! Retrieve strain energy per element
  etable,volu,volu            ! Retrieve volume per element
  sexp,w,sene,volu,1,-1       ! Calculate strain energy density

!ab_ratio=10
b=pts_rad
a=ab_ratio*b

num_nodes=9                   ! Set number of nodes on path
ptsBwNods=pts_rad/(h_psr/elm_thick)*ratio    !50    !*pts_rad/rad1          ! Set
number of points between nodes
path,jint_2D,num_nodes,50,ptsBwNods   ! Define path with name = "jint"


ppath,1,,crack_x+(-a/2),crack_y+(0),crack_z+(0),0
ppath,2,,crack_x+(-a/2),crack_y+(b/2),crack_z+(0),0
ppath,3,,crack_x+(0),crack_y+(b/2),crack_z+(0),0
ppath,4,,crack_x+(a/2),crack_y+(b/2),crack_z+(0),0
ppath,5,,crack_x+(a/2),crack_y+(0),crack_z+(0),0
ppath,6,,crack_x+(a/2),crack_y+(-b/2),crack_z+(0),0
```

```
ppath,7,,crack_x+(0),crack_y+(-b/2),crack_z+(0),0
ppath,8,,crack_x+(-a/2),crack_y+(-b/2),crack_z+(0),0
ppath,9,,crack_x+(-a/2),crack_y+(0),crack_z+(0),0

   pmap,UNIFORM,MAT             ! Select Uniform spacing of integration points, use
MAT command to consider material discontinuity
   pdef,w_sed,etab,w,NOAV          ! Put strain energy density on the path
   pcalc,intg,ja,w_sed,yg          ! Integrate energy w.r.t. global y
   *get,ja_tot,path,,last,ja     ! get final value of integral for 1st term of j


   pdef,uy,u,y,NOAV             ! put displacement uy on the path

   pvect,norm,nx,ny,nz          ! define the path unit normal vector
   pdef,sx,s,x,NOAV             ! put stress sx on the path
   pdef,sy,s,y,NOAV             ! put stress sy on the path

   pdef,sxy,s,xy,NOAV           ! put stress sxy on the path




   pcalc,mult,tx2,sxy,ny

   pcalc,add,tx_temp,tx1,tx2



   pcalc,mult,ty2,sy,ny          !   ty = sxy*nx + sy*ny + syz*nz
   pcalc,mult,ty3,syz,nz




   pcalc,mult,tz2,syz,ny          !   tz = sxz*nx + syz*ny + sz*nz
   pcalc,mult,tz3,sz,nz



   *get,dx,path,,last,s         ! define path shift
   dx=dx/(num_nodes*ptsBwNods)
   pcalc,add,xg,xg,,,,-dx/2      ! shift path from x to x-dx/2 (global x dir.)
   pdef,ux1,u,x,NOAV              ! define ux at x-dx
   pdef,uy1,u,y,NOAV              ! define uy at x-dx
```

```
   pdef,ux2,u,x,NOAV              ! define ux at x+dx
   pdef,uy2,u,y,NOAV              ! define uy at x+dx


   pcalc,add,xg,xg,,,,-dx/2      ! shift path back to original position
   pcalc,add,duxdx,ux2,ux1,1/dx,-1/dx     ! calculate derivative dux/dx
   pcalc,add,duydx,uy2,uy1,1/dx,-1/dx     ! calculate derivative duy/dx



   pcalc,mult,c2,ty,duydx          !   = tx*dux/dx + ty*duy/dx + tz*duz/dx

   pcalc,add,tdudx_temp,c1,c2
   pcalc,add,tdudx,tdudx_temp,c3

   pcalc,intg,jb,tdudx,s            ! form second integral (w.r.t. path length s)
   *get,jb_tot,path,,last,jb         ! get final value of integral for 2nd term of j
   jint_3D=abs(ja_tot-jb_tot)                ! add both terms
   jint_3D=jint_3D*1000      !  Get output units in J/m^2
   !PAGET,Jtab,TABLE             ! Output parameters for post processing verification
   !PDEF,STAT                   ! Show results in ANSYS
   !*STATUS,jint_23                ! Output the results of the J-integral calculation
   !pdef,clear                ! Clear old path
   !save                                ! Save work
!###############################################
Code

Code

Code
```

BIBLIOGRAPHY

[1] P. V. Guy V. Clatterbaugh, and Harry K. Charles, Jr., "Some Key Issues in Microelectronic Packaging," *John Hopkins API, Technical Digest,* vol. 20, p. 16, 1999.

[2] J. G. Robert Humfeld, "Mechanical Behavior of Adhesive Joints Subjected to Thermal Cycling," Master of Science, Engineering Mechanics, Virginia Polytechnic Institute and State University, Blacksburg, 1997.

[3] X. C. Shufong Zhao , Jinzhong Yao, "Impact of Hygroswelling and Vapor Pressure on Delamination," *IEEE,* p. 8, 2006.

[4] S. M. Wiederhorn, "Influence of Water Vapor on Crack Propagation in Soda Lime Glass," *Journal of the American Ceramic Society,* vol. 50, pp. 407-414, 1967.

[5] T. P. Ferguson, "Moisture and Interfacial Adhesion in Microelectronic Assemblies," PhD, Mechanical Engineering, Georgia Institute of Technology, Atlanta, Georgia, 2004.

[6] D. T. Rooney, "Failure Analysis of Die Bond Adhesion Failures Caused by Silicone Contamination," p. 10.

[7] C. Q. Cui, H. L. Tay, T. C. Chai, R. Gopalakrishan, and T. B. Lim, "Surface Treatment of Copper for the Adhesion Improvement to Epoxy Mold Compounds," presented at the 1998 Electronic Components and Technology Conference, 1998.

[8] H. Y. Lee and J. Yu, "Adhesion strength of leadframe/EMC interfaces," *Journal of Electronic Materials,* vol. 28, pp. 1444-1447, 1999.

[9] D. Broek, *Elementary Engineering Fracture Mechanics,* 3 ed.: Martinus Nijhoff Publishers, 1984.

[10] R. Lacombe, *Adhesion Measurement Methods: Theory and Practice,* 1 ed.: CRC Press, 2005.

[11] D. P. Miannay, *Fracture Mechanics,* 1 ed.: Springer, 1998.

[12] T. L. Anderson, *Fracture mechanics: fundamentals and applications*: CRC, 2005.

[13] J. Rice, "A path independent integral and the approximate analysis of strain concentration by notches and cracks," *Journal of Applied Mechanics,* vol. 35, pp. 379-386, 1968.

[14] X. Dai, M. V. Brillhart, and P. S. Ho, "Adhesion measurement for electronic packaging applications using double cantilever beam method," *Components and Packaging Technologies, IEEE Transactions on,* vol. 23, pp. 101-116, 2000.

[15] C. S. Bischof, "Relationship of Adhesion, Delamination, Preconditioning and Preplating Effects at the Plastic to Leadframe Interface," *IEEE,* pp. 827-834, 1995.

[16] L. K. Teh, M. Teo, E. Anto, C. C. Wong, S. G. Mhaisalkar, P. S. Teo, *et al.*, "Moisture-induced failures of adhesive flip chip interconnects," *IEEE*

Transactions on components and packaging technologies, vol. 28, pp. 506-516, 2005.

[17] X. Yan and R. K. Agarwal, "Two test specimens for determining the interfacial fracture toughness in flip-chip assemblies," *Journal of Electronic Packaging*, vol. 120, p. 150, 1998.

[18] I. Hofinger, M. Oechsner, H. A. Bahr, and M. Swain, "Modified four-point bending specimen for determining the interface fracture energy for thin, brittle layers," *International Journal of Fracture*, vol. 92, pp. 213-220, 1998.

[19] P. G. Charalambides, J. Lund, A. G. Evans, and R. M. McMeeking, "A test specimen for determining the fracture resistance of bimaterial interfaces," *Journal of Applied Mechanics*, vol. 56, p. 77, 1989.

[20] A. G. Evans, M. Ru, and B. J. Dalgeish, "The fracture energy of bimaterial interfaces," *Met. Trans. A*, vol. 21, pp. 2419-2429, 1990.

[21] H. C. Cao and A. G. Evans, "An experimental study of the fracture-resistance of bimaterial interfaces," *Mechanics of Materials*, vol. 7, pp. 295-304, Jun 1989.

[22] R. H. Dauskardt, M. Lane, Q. Ma, and N. Krishna, "Adhesion and debonding of multi-layer thin film structures," *Engineering Fracture Mechanics*, vol. 61, pp. 141-162, 1998.

[23] T.-C. H. Chang-Chun Lee, Chin-Chiu Hsia , Kuo-Ning Chiang, "Interfacial Fracture Investigation of Low-k Packaging Using J-Integral Methodology," *IEEE TRANSACTIONS ON ADVANCED PACKAGING,*, vol. 31, p. 9, 2008.

[24] D. J. L. Romeu. *Kolmogorov-Simirnov: A Goodness of Fit Test for Small Samples*. Available: http://www.theriac.org/DeskReference/viewDocument.php?id=200

[25] *Stats: One-Way ANOVA*. Available: https://people.richland.edu/james/lecture/m170/ch13-1wy.html